AGU PUBLICATIONS

Tectonics

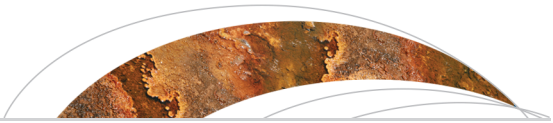

RESEARCH ARTICLE
10.1002/2014TC003690

Key Points:
- The Pamir Frontal Thrust initiated 5–6 Ma
- A regional kinematic shift in deformation occurred around 5–6 Ma
- Deposition of the piggyback basin is controlled by tectonics and climate

Supporting Information:
- Text S1, Figures S1–S4, and Tables S1 and S2

Correspondence to:
J. A. Thompson,
jessie.a.thompson@gmail.com

Citation:
Thompson, J. A., D. W. Burbank, T. Li, J. Chen, and B. Bookhagen (2015), Late Miocene northward propagation of the northeast Pamir thrust system, northwest China, *Tectonics*, *34*, 510–534, doi:10.1002/2014TC003690.

Received 22 JUL 2014
Accepted 8 FEB 2015
Accepted article online 11 FEB 2015
Published online 23 MAR 2015

Late Miocene northward propagation of the northeast Pamir thrust system, northwest China

Jessica A. Thompson[1], Douglas W. Burbank[1], Tao Li[2], Jie Chen[2], and Bodo Bookhagen[3]

[1]Department of Earth Science, University of California, Santa Barbara, California, USA, [2]State Key Laboratory of Earthquake Dynamics, Institute of Geology, China Earthquake Administration, Beijing, China, [3]Institute of Earth and Environmental Science, University of Potsdam, Potsdam-Golm, Germany

Abstract Piggyback basins on the margins of growing orogens commonly serve as sensitive recorders of the onset of thrust deformation and changes in source areas. The Bieertuokuoyi piggyback basin, located in the hanging wall of the Pamir Frontal Thrust, provides an unambiguous record of the outward growth of the northeast Pamir margin in northwest China from the Miocene through the Quaternary. To reconstruct the deformation along the margin, we synthesized structural mapping, stratigraphy, magnetostratigraphy, and cosmogenic burial dating of basin fill and growth strata. The Bieertuokuoyi basin records the initiation of the Pamir Frontal Thrust and the Takegai Thrust ~5–6 Ma, as well as clast provenance and paleocurrent changes resulting from the Pliocene-to-Recent uplift and exhumation of the Pamir to the south. Our results show that coeval deformation was accommodated on the major structures on the northeast Pamir margin throughout the Miocene to Recent. Furthermore, our data support a change in the regional kinematics around the Miocene-Pliocene boundary (~5–6 Ma). Rapid exhumation of NE Pamir extensional domes, coupled with cessation of the Kashgar-Yecheng Transfer System on the eastern margin of the Pamir, accelerated the outward propagation of the northeastern Pamir margin and the southward propagation of the Kashi-Atushi fold-and-thrust belt in the southern Tian Shan. This coeval deformation signifies the coupling of the Pamir and Tarim blocks and the transfer of shortening north to the Pamir frontal faults and across the quasi-rigid Tarim Basin to the southern Tian Shan Kashi-Atushi fold-and-thrust system.

1. Introduction

Basins on the margins of orogens and plateaus provide records of deformation and erosion of the surrounding ranges, e.g., *Heermance et al.* [2007, 2008], *Talling et al.* [1995], *Jordan et al.* [1988], *Paola et al.* [1992], and others. Exhumation in the hinterland or local motion on a thrust fault may be recorded as rotated unconformities, growth strata, and changes in sediment provenance, sediment-accumulation rate, and/or depositional environments within basin sediments [*Riba*, 1976; *Jordan et al.*, 1988; *Burbank and Raynolds*, 1988; *Talling et al.*, 1995]. In particular, piggyback basins located in the hanging walls of active structures [*Ori and Friend*, 1986; *DeCelles and Giles*, 1996] have the potential to provide a detailed record of local structural and stratigraphic evolution on nearby faults [*Suppe et al.*, 1997; *Hubert-Ferrari et al.*, 2007; *Charreau et al.*, 2008]. High-resolution dating of the basin fill, detailed documentation of stratigraphic facies, and paleocurrent and provenance changes within a piggyback basin can quantify the growth of an orogen [e.g., *Heermance et al.*, 2007; *Lease et al.*, 2011].

On the northeastern margin of the Pamir orogen in NW China (Figures 1 and 2), the Pamir Frontal Thrust (PFT) and the Takegai Thrust (TT) represent the active deformation boundary [*Chen et al.*, 2011; *Li et al.*, 2012; *Sobel et al.*, 2013]. To date, little is known about the timing of Cenozoic deformation along these major fault systems [*Sobel and Dumitru*, 1997; *Sobel et al.*, 2011, 2013]. Here we date the onset of thrusting along the PFT and TT faults by exploiting the structure and stratigraphy in the Bieertuokuoyi piggyback basin located in the hanging wall of the Pamir Frontal Thrust. Integrating field observations and stratigraphic changes in conjunction with magnetostratigraphy and cosmogenic burial dating within the piggyback basin, we date the formation and deposition of growth strata that are directly linked to both the Takegai Thrust and the Pamir Frontal Thrust faults. Our results provide new insights into the Neogene tectonic evolution of the Pamir-Tian Shan region and the timing of outward growth of the Pamir orogen.

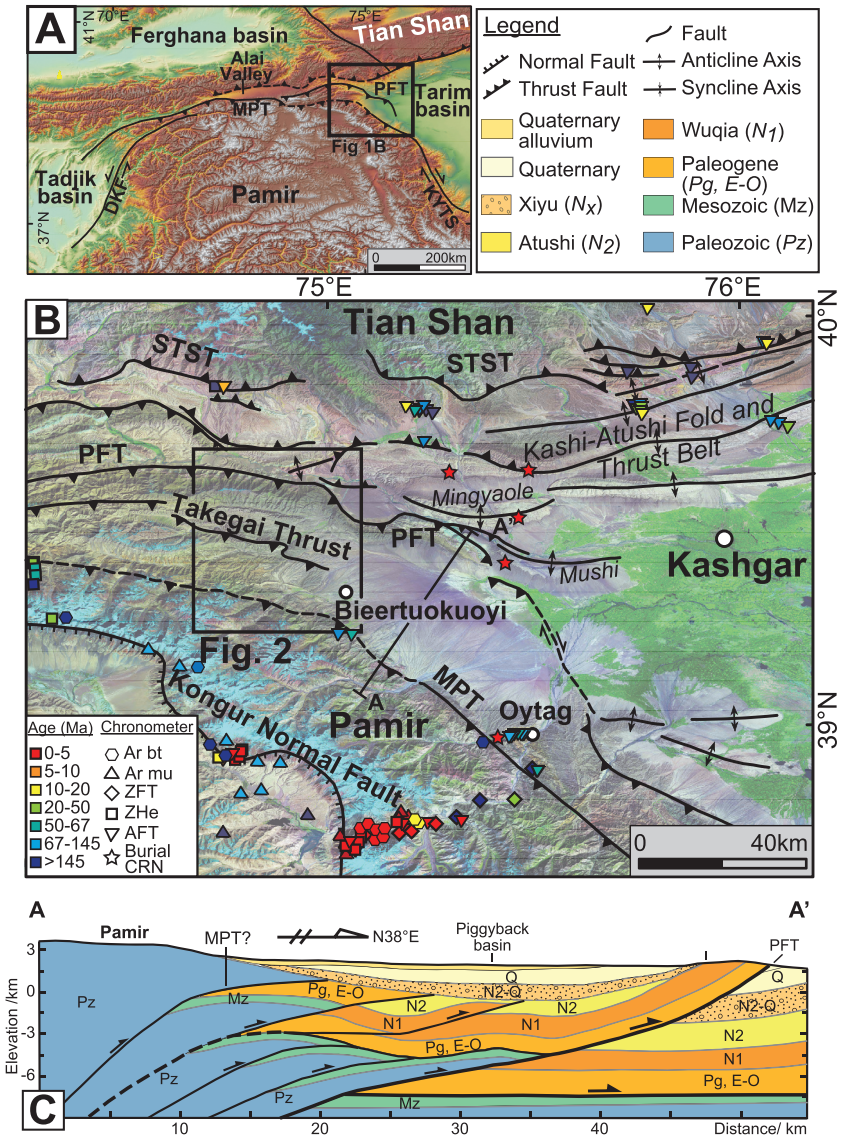

Figure 1. (a) Digital elevation model of the Pamir Plateau, the southern Tian Shan, and the westernmost Tarim Basin. (b) Advanced Spaceborne Thermal Emission and Reflection Radiometer (ASTER) scene of the NE Pamir Margin, illustrating major structures, chronologic data, and location of cross section in Figure 1c. Chronologic data consists of low-temperature thermochronology from *Sobel et al.* [2013, and references therein], *Cao et al.* [2013b], *Thiede et al.* [2013], and *Sobel and Dumitru* [1997], and cosmogenic burial ages from *Thompson* [2013]. Ar mu—$^{40}Ar/^{39}Ar$ muscovite, ZFT—zircon fission track, ZHe—zircon (U-Th)/helium, AFT—apatite fission track, and burial CRN—cosmogenic radionuclide burial age. (c) Modified balanced cross section (A-A') [*Chen et al.*, 2010; *Li et al.*, 2012] based on a seismic line crossing the MPT, modern-day piggyback basin, and PFT. Legend for unit colors in Figure 1a. DKF—Darvas-Karakul Fault, KYTS—Kashgar-Yecheng Transfer System, MPT—Main Pamir Thrust, PFT—Pamir Frontal Thrust, and STST—South Tian Shan Thrust.

2. Geologic Setting

The Pamir salient is the northwestern continuation of the Tibetan Plateau (Figure 1a) and formed as a result of the Indo-Eurasian collision [*Burtman and Molnar*, 1993]. Peaks exceeding 7000 m punctuate the edge of the Pamir around a high-elevation, low-relief interior. The topography at the edge of the plateau drops several thousand meters to the north into a foreland basin that lies at the western edge of the Tarim Basin between the Pamir and the Tian Shan Mountains to the north. During the Cenozoic, the northern Pamir has indented northward ~300 km relative to stable Eurasia as the Eurasian crust subducted southward beneath the Pamir [*Burtman and Molnar*, 1993]. Synchronously with indentation,

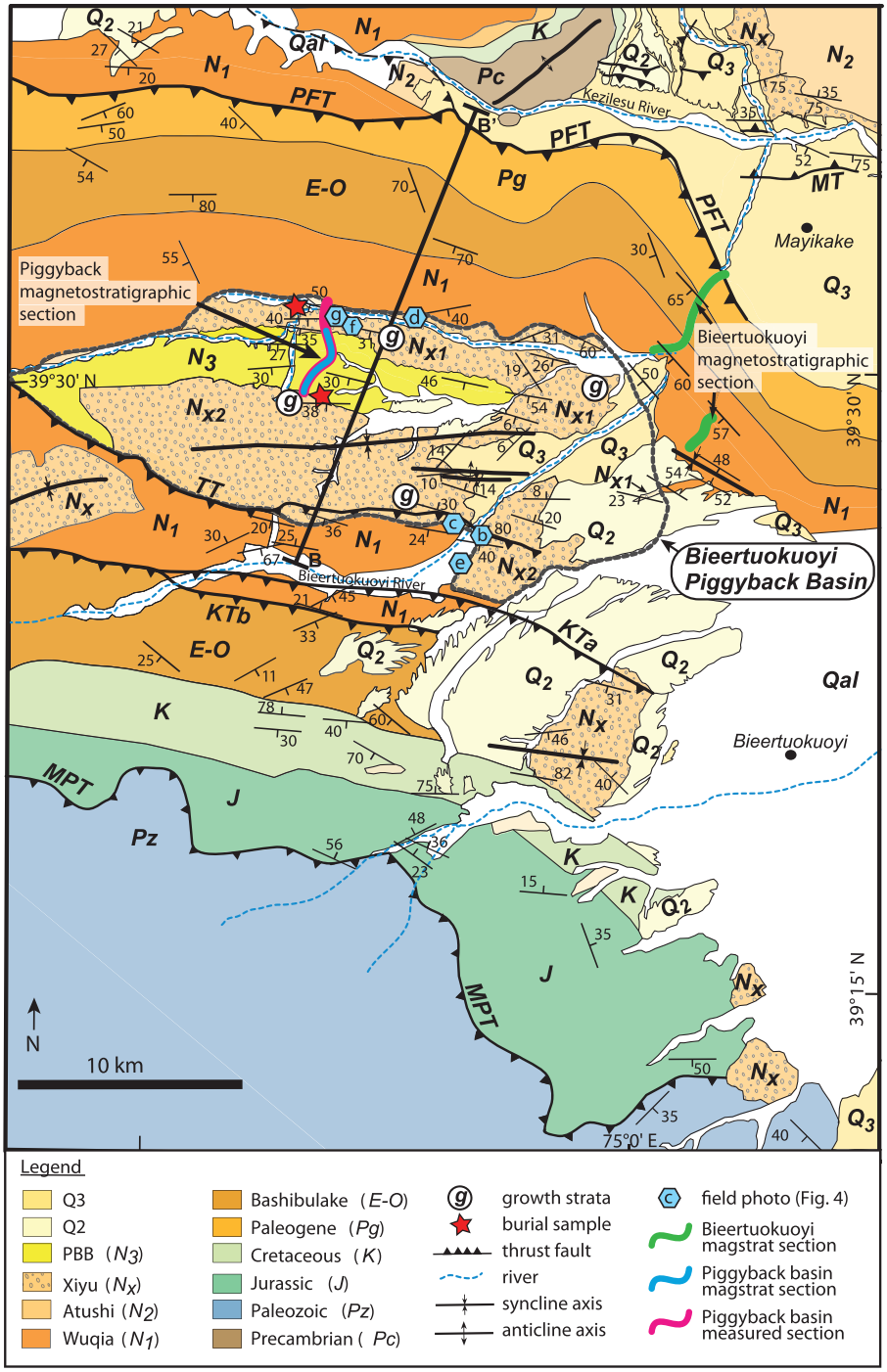

Figure 2. Geologic map of the NE Pamir, created from our field mapping and modified from *Xinjiang Bureau of Geology and Mineral Resources* [1993]. KT—Kenenbieerte Thrust (a and b represent faults within the KT fault zone), MPT—Main Pamir Thrust, MT—Mayikake Thrust, PFT—Pamir Frontal Thrust, STST—South Tian Shan Thrust, TT—Takegai Thrust. See Table S1 for descriptions of Tertiary units. For clarity, smaller-scale structures in Eo-Oligocene and Cretaceous strata in the hanging wall of the TT are not shown. Blue polygons show locations of field photos in Figure 4.

nearly 300 km of crustal shortening and significant crustal thickening occurred along a series of sinistral and dextral strike-slip faults on the eastern and western margins, respectively, along with thrusting on the northern margin (Figure 1a) [*Burtman and Molnar*, 1993; *Sobel et al.*, 2011] where several thrust faults, including the Main Pamir Thrust (MPT) and the Pamir Frontal Thrust (PFT), facilitate the outward

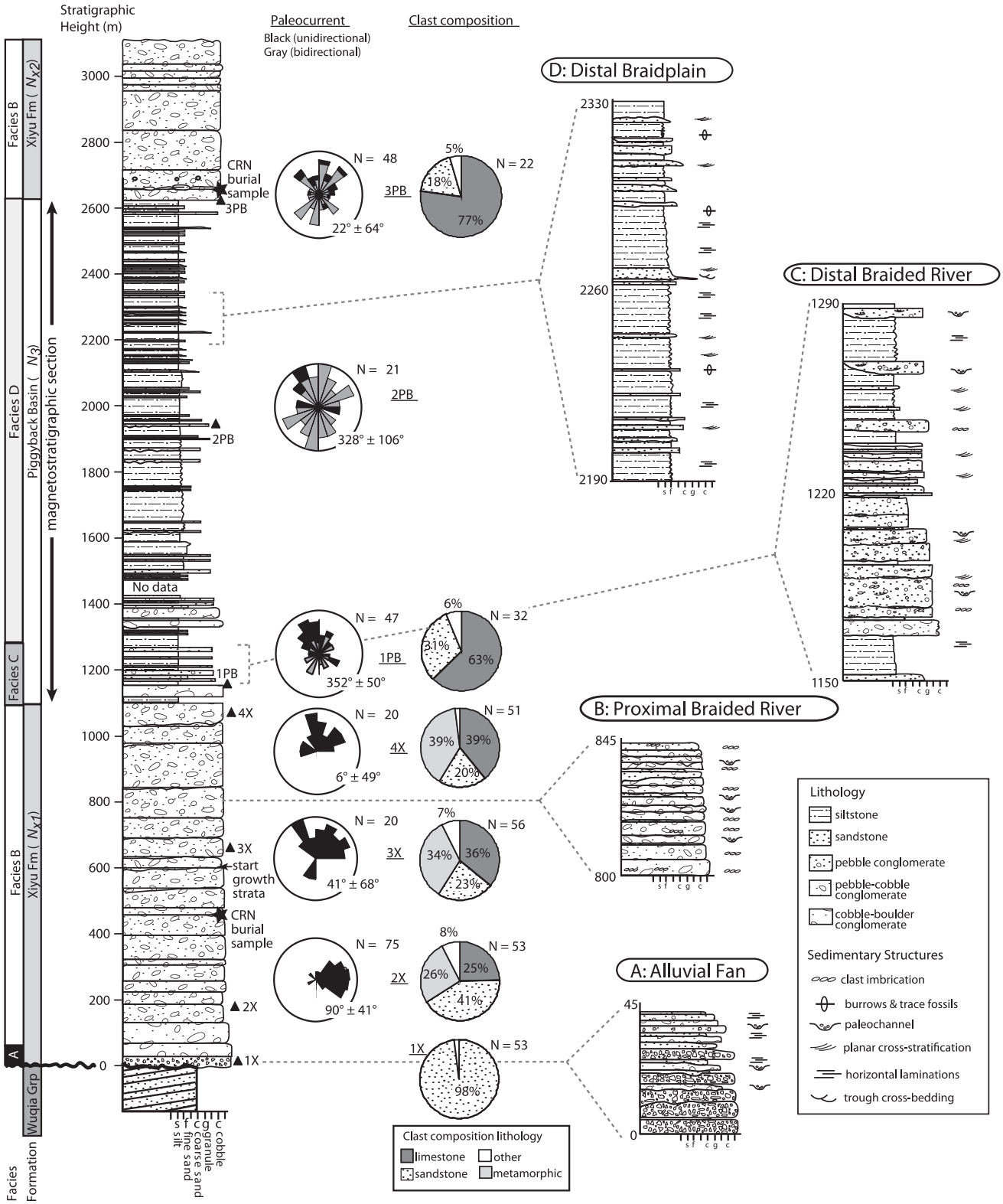

Figure 3. Lithologies, interpreted depositional facies and units, paleocurrent directions, and clast counts within the measured magnetostratigraphic section. Expanded columns A to D illustrate typical facies assemblages for each depositional environment (see Table 2). For paleocurrents, black fill indicates unidirectional flow indicators, and grey fill indicates bidirectional flow indicators and are additive. Average and 1σ errors on paleocurrent direction are listed adjacent to the rose diagram and were calculated using unidirectional paleocurrent data only. Black triangles next to section mark locations on clast counts and paleocurrent measurements. Black stars note location of cosmogenic burial samples within the section.

Table 1. Lithofacies Codes and Interpretations[a]

Facies Code	Lithofacies Description	Interpretation
Fl	siltstone and fine-grained sandstone with fine laminations and/or small ripples	overbank or waning flood deposits
Fb	siltstone and fine-grained sandstone, laminated to massive, and bioturbation and mottling common	overbank deposits
Sh	fine- to medium-grained sandstone with plane parallel laminations	deposition under planar bed flow (upper and lower regime)
Sp	fine- to coarse-grained sandstone with planar cross stratification	migration of 2-D ripples under unidirectional lower flow regime
St	fine- to coarse-grained sandstone with trough cross stratification	migration of 3-D ripples under unidirectional lower flow regime
Sr	fine- to medium-grained sandstone with ripples	migration of 2-D and 3-D ripples under unidirectional lower flow regime
Gms	pebble conglomerate and matrix supported with subrounded to rounded pebbles within a medium- to coarse-grained sand matrix	debris flow deposits within channels and pebble lag within channels
Gm	massive, clast-supported pebble to boulder conglomerate, unstratified, and poorly sorted	deposition from clast-rich debris flows
Gci	pebble to cobble conglomerate, clast-supported, horizontally stratified, and imbricated	deposition in longitudinal bars and gravel sheets

[a]Modified after *Miall* [1978, 1985], *Decelles et al.* [1991b].

growth of the orogen (Figure 1b) [*Chen et al*., 1997, 2011; *Sobel and Dumitru*, 1997; *Li et al*., 2012; *Sobel et al*., 2013].

The Pamir Plateau is an amalgamation of terranes that are the along-strike equivalents of Himalayan and Tibetan plateau tectonic terranes, accreted to the southern front of Eurasia during the Mesozoic and Paleozoic [*Burtman and Molnar*, 1993; *Robinson et al*., 2004; *Schwab et al*., 2004]. By ~50 Ma, the Pamir Plateau had substantially thickened crust [*Ducea et al*., 2003; *Hacker et al*., 2005] as a result of the Indo-Eurasian collision.

Low-temperature thermochronology from the interior and margins of the Pamir Plateau suggest exhumation and shortening initiated in the middle to late Paleogene and continues to the present (Figure 1b) [*Sobel and Dumitru*, 1997; *Yin et al*., 2002; *Amidon and Hynek*, 2010; *Thiede et al*., 2013; *Cao et al*., 2013b]. Along the northern margin of the Pamir, in the Alai valley (Figure 1a), shortening began during the Oligo-Miocene and continues to the present [*Strecker et al*., 1995; *Coutand et al*., 2002]. Farther west, where the Pamir and Tian Shan are already juxtaposed, the collision began as late as the Mio-Pliocene [*Pavlis et al*., 1997].

During the Miocene to present, deformation along the northeastern margin of the Pamir has been concentrated on thrust faults, including the Main Pamir, Kenenbieerte, Takegai, and the Pamir Frontal thrusts, that bound the plateau and the foreland basin (Figures 1b and 1c) [*Sobel and Dumitru*, 1997; *Sobel et al*., 2011; *Li et al*., 2012]. Based on detrital low-temperature thermochronology near the town of Oytag (Figure 1b), the Main Pamir Thrust (MPT) initiated 25–18 Ma [*Sobel and Dumitru*, 1997; *Bershaw et al*., 2012]. Similarly, stratigraphic and detrital zircon provenance changes near the MPT suggest that exhumation on the MPT was underway by the early or middle Miocene (Figure 1b) [*Bershaw et al*., 2012]. Notably, the slip rate is inferred to have slowed during the late Miocene or Pliocene [*Sobel and Dumitru*, 1997; *Sobel et al*., 2011]. Sparse seismic activity and low-convergence rates from geodetic studies indicate a low modern slip rate ($<$1 mm/a) on the MPT on the northeastern Pamir margin [*Yang et al*., 2008; *Zubovich et al*., 2010; *Li et al*., 2012; *Ischuk et al*., 2013]. Minimum average shortening rates since the Miocene along the bounding fault of the Trans Alai Range, the westward continuation of the MPT (Figure 1a), are 0.7–0.8 mm/a [*Coutand et al*., 2002], whereas Holocene slip rate averages are as high as ~6 mm/a [*Arrowsmith and Strecker*, 1999]. The Pamir Frontal Thrust (PFT), spatially separated from the MPT by ~30 km, is the northernmost structure of the Pamir. The PFT accommodates nearly all of the late Quaternary deformation along the northeast margin of the Pamir, with average shortening rates of 6–8 mm/a since ~0.35 Ma [*Li et al*., 2012].

The Bieertuokuoyi piggyback basin is located ~75 km west of Kashgar, within the Cenozoic foreland basin between the Pamir and Tian Shan ranges (Figures 1b and 2). The foreland basin contains up to 9 km of Cenozoic

Table 2. Lithofacies Associations and Descriptions

Facies	Lithofacies	Characteristics	Interpretation
A	Gm	Disorganized, clast-supported conglomerates with no internal stratification	Debris flows initiated on steep local slopes or alluvial fans, with rapid deposition into a braided river system
B	Gci and Sh	Multistory packages of imbricated conglomerates with uncommon isolated, horizontally stratified sandstones	Gravel bars and channel-fill sands deposited in a proximal braided river
C	Gci, Sh, St, Sp, Sr, and Fl	Multistory packages of imbricated conglomerates with horizontally and cross-stratified, and rippled sandstones and laminated siltstones	Gravel bars and channel-fill sands deposited in a distal braided river
D	Fb, Fl, Sh, Gms, Sr, and Sp	Laminated or massive bioturbated siltstones, laminated or cross-stratified sandstones with uncommon, and isolated matrix-supported pebble conglomerates	Sheet sands and low-energy flows deposited in a distal braid plain

strata (Table S1) [*Jia et al*., 2004; *Heermance et al*., 2007], of which the Bieertuokuoyi piggyback basin comprises the uppermost 3 km.

3. Stratigraphy of the Bieertuokuoyi Piggyback Basin

To the northwest of the town of Bieertuokuoyi, we described ~3000 m of Neogene sedimentary rocks in the Bieertuokuoyi basin and measured ~1600 m in detail in conjunction with the magnetostratigraphic sampling (Figures 2 and 3). This piggyback basin lies between the major faults of the region: the Main Pamir Thrust and the Pamir Frontal Thrust. The basin itself is interpreted to record the uplift of ranges associated with these faults (Figures 1 and 2).

3.1. The Wuqia Group

Directly underlying the base of the piggyback succession (Figures 1c and 2 and Table S1 in the supporting information), the Wuqia Group is over 3000 m thick and consists of interbedded grey-green to light blue, medium-to-coarse sandstones and red-brown mudstones and siltstones. Sandstone beds are 20 cm to 1 m thick, with erosional lower contacts, rare rip-up clasts of the underlying siltstone/mudstone, and abundant epsilon cross bedding. Siltstone and mudstone beds are 5 to 20 cm thick with bioturbation and trace fossils, whereas groups of these beds can be over 5 m thick. The Wuqia Group is interpreted to have been deposited in a low-energy meandering stream environment in which migrating sandstone channels cut into a mudstone/siltstone-dominated floodplain [*Miall*, 1996]. In the western Tarim Basin, the Wuqia Group spans the Miocene, based on magnetostratigraphy and biostratigraphy (Table S1) [*Chen et al*., 2002; *Yin et al*., 2002; *Jia et al*., 2004; *Heermance et al*., 2007]. At the top of the Wuqia Group, an angular unconformity marks the base of the Bieertuokuoyi piggyback basin.

3.2. The Bieertuokuoyi Piggyback Basin Section

We divided the Bieertuokuoyi section itself into four lithofacies units, based on lithology, sedimentary structures, and interpreted depositional environment. The lithofacies that define the basin's overall stratigraphy are interpreted to represent deposition from alluvial fans to distal, sandy braided rivers (Tables 1 and 2). Facies A (0–45 m, Figures 3 and S1a and Table 2) is a poorly sorted, clast-supported, cobble-boulder conglomerate with a medium-to-coarse reddish sand matrix. Facies A unconformably overlies the Wuqia Group, with relief of up to 50 m in paleovalleys along its basal contact. This lithofacies is similar to the proximal deposits of the Xiyu conglomerate found in other regions of the NW Tarim Basin, as described by *Heermance et al*. [2007, 2008]. The subangular to subrounded clasts are up to 3 m in diameter. Clasts comprise red, green, and pink sandstones and siltstones that are similar in appearance to and likely derived from the underlying Wuqia Group. Conglomerate beds are massive, 2–10 m thick, clast-supported, lenticular and discontinuous, and they uncommonly have erosive lower boundaries (Gm, Table 1). The thickness of this facies varies considerably along strike: it pinches out completely to the west and thickens eastward. The presence of large, subangular, monolithologic clasts and the lack of clast imbrication, sedimentary structures, or obvious channelization suggest facies A represents deposits of proximal

alluvial fans (Table 2) [*Blair and McPherson*, 1992, 1994] that are likely derived from locally high relief [e.g., *DeCelles et al*., 1991a, 1991b].

Approximately 10 km east of the measured section, facies A interfingers with facies B. Compared to facies A, facies B displays smaller mean clast size and more abundant fine-scale sedimentary structures. Facies A and B are gradational and interfinger over a thickness of ~20 m. Facies B records a major shift in the provenance and paleocurrents, thereby suggesting some drainage reorganization on the NE Pamir margin. Clast-supported, pebble-cobble conglomerates dominate facies B (40–1090 m, 2620–3000+ m, Figures 3 and S1b and Table 2). Clasts are well sorted, subrounded, and well imbricated (Gci, Tables 1 and 2) within a poorly sorted matrix of sand and silt. Boulder clasts are rare within beds in the lower few hundred meters, but clast size and roundness generally increases up section. Conglomerate beds are lenticular, discontinuous, and 2–10 m thick. Bed contacts are commonly irregular with channels that incise up to 0.5 m into the underlying beds. Sandstone clasts (compositionally identical to clasts in facies A and likely derived from the underlying Wuqia Group) have a dominant presence in the lower 500 m of the section. Limestone, granitic, and metamorphic clasts are more abundant in the upper 500 m of facies B. From bottom to top, limestone and metamorphic clasts increase from ~25% to 39% each, whereas sandstone clasts decrease from 41% to 20%. Some conglomerate beds in the lower 400 m consist entirely of subrounded clast-supported sandstone boulders. The conglomerates are interbedded with uncommon, lenticular 0.5 to 1 m thick, medium- or coarse-grained sandstone beds. The sandstone beds commonly contain horizontal laminations (Sh, Table 1).

We interpret the pebble-boulder conglomerate to have been deposited in a braided fluvial environment with a very minor accumulation of channel-fill sands (Table 2) [*Miall*, 1996; *Jones et al*., 2001; *Limarino et al*., 2001; *Nichols and Fisher*, 2007]. Channel-fill sandstones (Sh, Table 1) are interpreted to have been deposited during waning stream flow, filling scours in gravel bars [*Uba et al*., 2005]. These channelized conglomerates with common basal scours are likely somewhat distal from their source area, given the size, rounding, and sorting of the clasts [*Paola et al*., 1992]. Paleocurrent directions are west to east in the lower 400 m of the facies B and south to north in the upper 400 m of facies B (Figure 3). We suggest the paleocurrent change and the gradual increase of limestone, granitic, and metamorphic clasts in the upper section record uplift of source areas [*Burtman and Molnar*, 1993; *Schwab et al*., 2004; *Robinson et al*., 2004] in the Pamirs to the south.

Facies B transitions gradually into facies C (1090–1250 m, Figures 3 and S1c), which has a higher percentage of sandstones and siltstones and fewer conglomerate beds than facies B. Facies C is an interbedded sequence of reddish-brown, clast-supported, pebble to boulder conglomerates (Gci, Table 1), red-brown, fine- to coarse-grained sandstone beds, and buff, 5 to 10 cm thick siltstone beds (Sh, St, and Sp, Tables 1 and 2). In facies C, conglomerate beds are 3–20 m thick, and although individual bedding thickness changes along strike, groups of stacked beds can be traced laterally for kilometers. Clasts are commonly 2–20 cm in diameter and are subrounded to rounded within a poorly sorted sand and silt matrix. Clast compositions include a higher percentage of limestone clasts and fewer sandstone or metamorphic clasts compared to facies B. Clast imbrication and channel cut-and-fill structures are common. Beds typically have sharp erosive bases with ~20 cm to 1 m of local incision into underlying siltstone and sandstone beds with rare rip-up clasts along the contact. The siltstone and fine sandstone beds are 2–10 cm thick and lenticular in shape with sharp contacts. Ripples and both planar and trough cross stratification are common (Sh, St, Sp, Sr, and Fl, Table 1). Bioturbation is present near the tops of siltstone beds (Fb, Table 1).

We interpret this environment as a transition to a distal braided river, with finer-grained deposits that may be overbank or bar deposits (Table 2) [*Miall*, 1985; *Collinson*, 1996]. Laminated silt beds (Fl and Fb, Table 1) were deposited from suspension on the fluvial floodplains during waning flow conditions [*Miall*, 1996; *Jones et al*., 2001]. Paleocurrent directions indicate a south-to-north transport direction (Figure 3). The transition to an increasing percentage of finer-grained beds may indicate either a relative quiescence of uplift within the source area, creating a more distal braided river facies or ponding behind a growing structure.

Facies D (1250–2620 m, Figures 3 and S1d) is dominated by grey-yellow and red-brown siltstones with uncommon (10–15%) fine to coarse sandstones with beds 5 to 10 cm thick. The presence of abundant siltstone beds and lack of conglomerate beds distinguishes facies D from facies C. Fine-grained sandstone beds are commonly tabular with planar contacts, and most have planar cross stratification or horizontal laminations 1–2 mm thick (Sp and Sh, Table 1). Burrows and additional forms of bioturbation are commonly present near the tops of fine-grained sandstone and siltstone beds (Fb, Table 1). The siltstones and fine

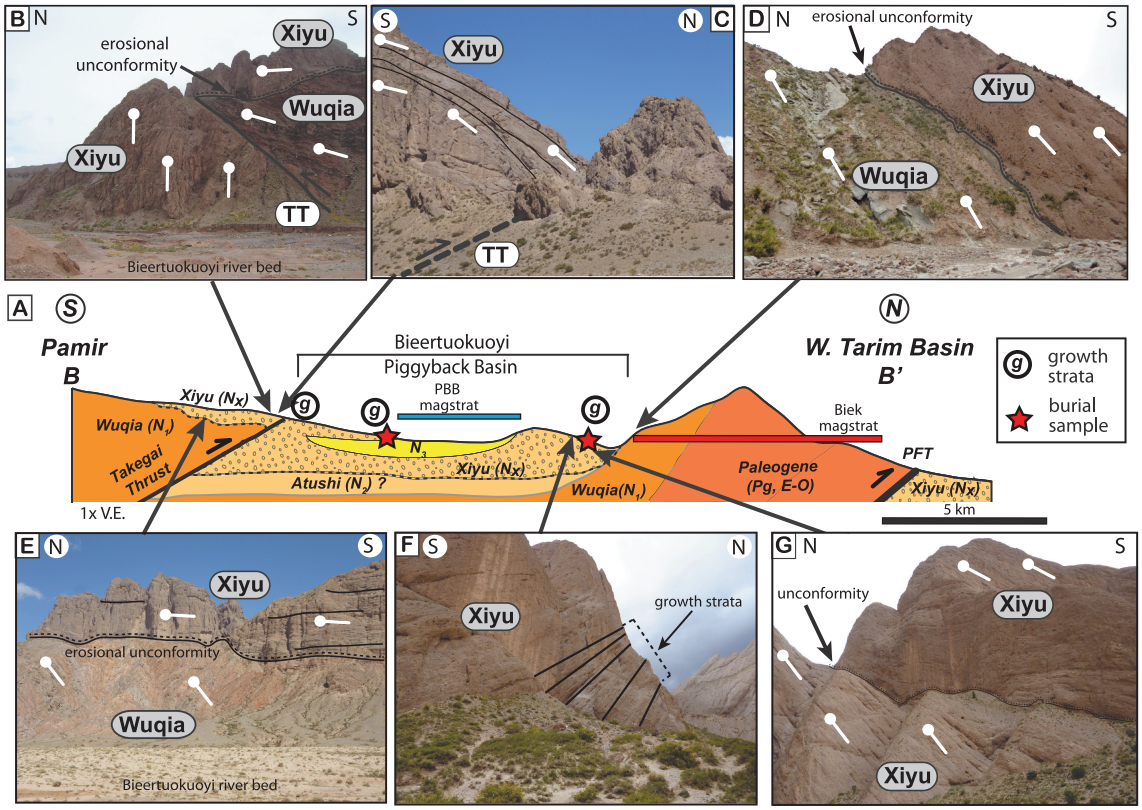

Figure 4. Field photos of growth strata and structures at the base of the Bieertuokuoyi Basin and the Takegai Thrust (TT) along a (a) schematic geologic cross section (B-B', see Figure 2 for location). Circled g represents growth strata. Red stars mark locations of the burial samples. Colored bars represent approximate locations of magnetostratigraphic sections. (b) Takegai Thrust, placing Wuqia Group over Xiyu, and with Xiyu (N_{x2}) deposited on top of Wuqia Group. (c) Growth strata in the Xiyu Formation (N_{x2}) draping over the fault tip of the TT (dashed line). The Bieertuokuoyi piggyback basin is to the north. (d) Erosional unconformity at the base of the basin, with Xiyu Formation (N_{x1}) deposited on top of Wuqia. (e) Erosional unconformity between the Wuqia Group and Xiyu Formation (N_{x2}) in the hanging wall of the TT. The TT is to the left of the photo. (f) Fanning dips and thickening beds and (g) minor angular unconformities within the Xiyu Formation (N_{x1}). Symbols and lithology colors are the same as Figure 2.

sandstones are interbedded with 0.3 to 1 m thick coarse-grained sandstone and pebble conglomerate beds and are lenticular on scales of tens to hundreds of meters. Most coarse-grained sandstone beds have an erosive base with up to 30 cm of relief and commonly display rip-up clasts and cross beds along the contact. The pebble conglomerates are matrix supported with subrounded to rounded pebbles within a medium- to coarse-grained sand matrix (Sm, Table 1). The coarse sandstone and pebble conglomerate beds commonly fine upward into fine-grained sandstone over intervals of 1–5 m. The fine sandstones near the tops of these beds commonly have ripples or planar cross stratification (Sr and Sp, Table 1). We interpret this facies as a distal braid plain (Table 2) [*Miall*, 1977; *Vos and Tankard*, 1981; *Miall*, 1985; *Zheng et al.*, 2000] at the basinward end of an alluvial fan. A lack of channels and tabular, fine-grained units provide evidence for sheet flow, whereas sandstone and pebble conglomerates may represent deposits from infrequent, higher-discharge events [*Miall*, 1977].

In summary, the piggyback basin section is interpreted to comprise two different fluvial depositional environments. Facies A, similar to proximal Xiyu deposits in other parts of the Tian Shan foreland [*Heermance et al.*, 2007], is interpreted as proximal alluvial fan deposits. Facies B–D are interpreted to represent proximal and distal braided fluvial deposits. Facies B, analogous to the typical Xiyu Formation within the western Tarim Basin [*Chen et al.*, 2002; *Heermance et al.*, 2007, 2008; *Charreau et al.*, 2009] was deposited by gravelly braided rivers. Facies C is a more distal facies of a braided river deposit with increasing fines that transition into Facies D, a distal braid plain. The changes in dominant paleocurrent direction (from west to east to south to north) and in clast composition (from sandstone to limestone) (Figure 3), within the lower 1200 m of the section, are interpreted as a response to the initiation of uplift and erosion of a carbonate-bearing source area in the Pamir to the south. A gradual fining upward sequence through the lower half of the basin,

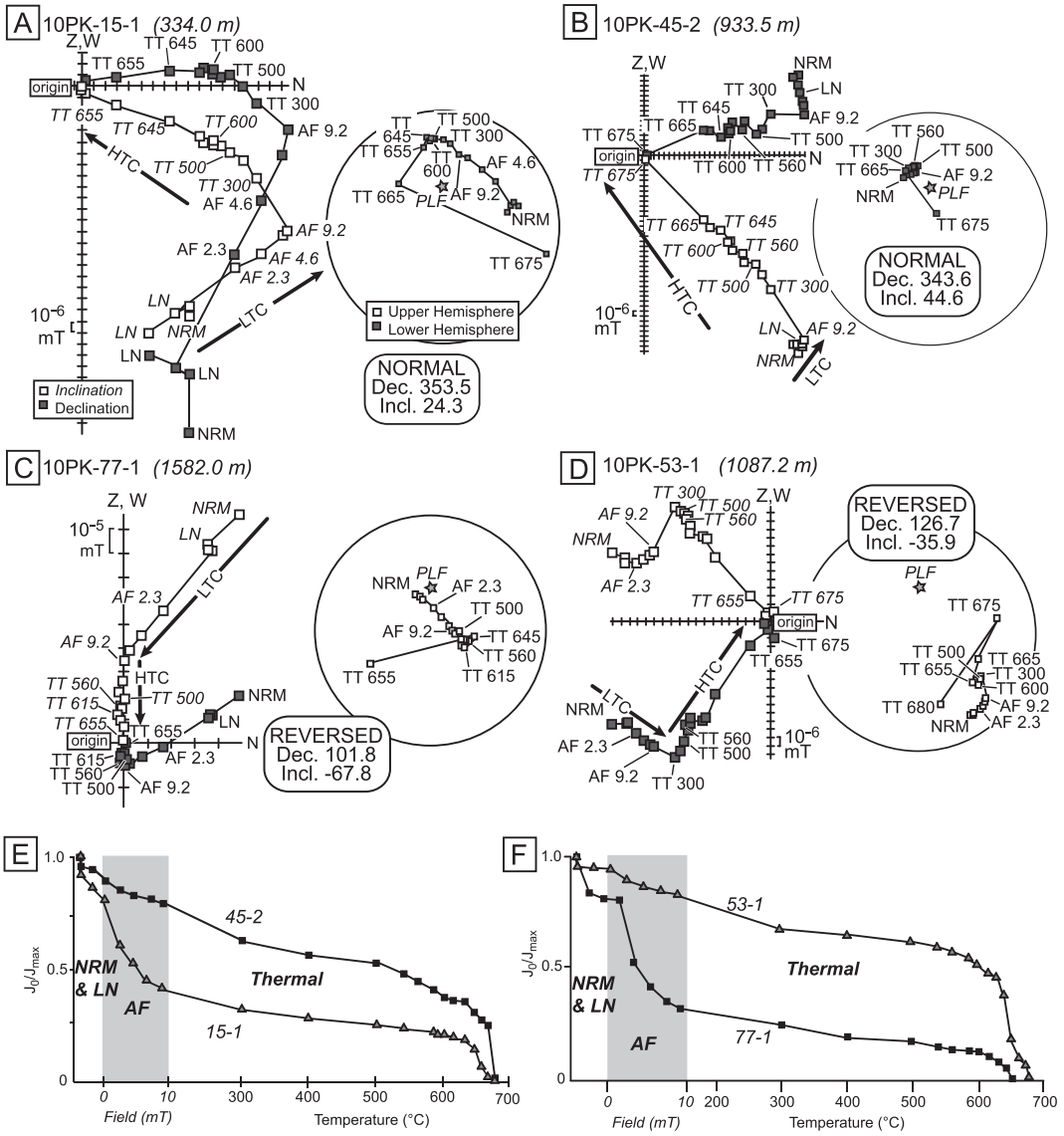

Figure 5. (a–d) Representative examples of paleomagnetic results using stepwise alternating field and thermal demagnetization of selected oriented samples. Zijderfeld and equal area plots are shown, with some of the steps labeled. Most samples displayed multiple temperature components, and examples of the low-temperature component (LTC) and high-temperature component (HTC) are of the ChRM are shown. (e, f) Plots showing the decay of the magnetic moment for the same samples in Figures 5a–5d. NRM = natural remanent magnetization, LN = low-temperature step (when samples were cooled in liquid nitrogen), and AF = alternating field (in mT). Both magnetite and hematite are interpreted as ChRM carriers, noted by the decrease in magnetic moment between 500° and 580°C and between 660° and 680°C.

from a cobble-dominated conglomerate (Facies B) to thick series of interbedded siltstone and sandstone beds (Facies D), may be a response to sedimentary ponding behind the growing topography above the Pamir Frontal Thrust to the north. The thin stratigraphic successions and the unconformity at the base of the section are consistent with sedimentation in a piggyback basin setting [e.g. *Ori and Friend*, 1986].

4. Field Mapping Observations and Interpretations

4.1. Main Pamir Thrust

The MPT (Figures 1c and 2) places Paleozoic metasediments over Mesozoic sedimentary rocks. Where observed in the field near the town of Oytag (Figure 1b), the MPT is not a discrete fault surface; rather, it is a ~200 m to ~1 km thick zone of fractured and brecciated rocks with abundant quartz veins. The fault zone as a whole

appears to dip steeply to the south, although individual fractures and quartz veins dip to the north. We observed growth strata at two locations near the MPT: one set at a syncline related to a smaller fault in front of the MPT, and another set within a Pleistocene (?) alluvial fan overlying Neogene sediments in the footwall of the MPT. We did not observe any offset of late Pleistocene or Holocene geomorphic surfaces, suggesting the fault has not ruptured the surface since the late Pleistocene.

4.2. Takegai and Kenenbieerte Thrusts

The Takegai Thrust (TT) and Kenenbieerte Thrust (KT) fault zone is located ~15 km to the north of the Main Pamir Thrust and 20 km to the south of the Pamir Frontal Thrust at the southern end of the Bieertuokuoyi piggyback basin (Figure 2) and is at least 5 km wide. The fault zone has three larger individual faults (Takegai Thrust and the Kenenbieerte Thrust (a and b), Figure 2) and numerous smaller faults that we observed but did not map in detail. In the hanging wall of the northernmost Takegai Thrust (Figures 2 and 4a), the Miocene Wuqia Group (Table S1) is highly deformed into a series of small-scale folds and faults with no dominant vergence. Separated by an angular unconformity, the Xiyu Formation (N_{x2}) overlies the Wuqia Group, does not exhibit such mesoscale deformation (Figures 4b and 4e) and, therefore, postdates the earlier deformational episode. This earlier deformational episode is probably not a result of movement on the Takegai Thrust but instead may have been caused by the Kenenbieerte Thrust or unknown smaller faults to the south of the Takegai Thrust. The Xiyu Formation is also present in the footwall of the Takegai Thrust. The bedding is nearly vertical and in some locations, overturned and dipping to the south. Where we observed the fault at the Bieertuokuoyi water gap, the Wuqia Group and Xiyu Formation are thrust directly over vertically dipping Xiyu on an E-W striking fault that dips ~30° to the south (Figure 4b). The Xiyu Formation (N_{x2}) in the hanging wall drapes over the tip of the fault, creating growth strata into the footwall of the thrust (Figure 4c). These observations indicate that the TT underlying the fold ruptured the surface during Xiyu deposition, yet deposition of the Xiyu Formation occurred both during and after movement on the TT.

Along a valley ~5 km south of the Takegai Thrust, a faulted anticline places the Eo-Oligocene Bashibulake Formation (Table S1) over the Wuqia Group (Figure 2) along the KTb. Given that the Paleocene is missing from the section south of the Bieertuokuoyi River yet is present within this section along strike, another fault may be present placing Cretaceous sandstones over the Eo-Oligocene rocks. A series of E-W trending, faulted anticlines and synclines within the Cretaceous and Eo-Oligocene formations crop out south of the Bieertuokuoyi River (Figure 2), but, due to access restrictions, this area was only mapped at a reconnaissance scale, and our interpretations should be considered preliminary.

Approximately 20 km east of the Bieertuokuoyi River (Figure 2), strands of the KTa appear as a series of imbricate thrust faults with a spacing of <2 km. Although a cover of Quaternary sediments prevents a detailed analysis of these structures, ~30° south dipping faults place folded rocks of the Eo-Oligocene Bashibulake Formation over the Xiyu Formation.

4.3. Pamir Frontal Thrust

Near the Bieertuokuoyi River, the PFT dips approximately 75° to the south and places Paleogene gypsum and marine sediments over Quaternary fluvial gravels (Figure 2). Recent exposure of the fault reveals slickenlines with a rake of 34° to the northwest [*Li et al*., 2012]. Within the Paleogene formations, numerous faults and folds were mapped using aerial imagery, Google Earth, and reconnaissance field mapping. Farther east, the PFT thrusts Paleogene formations over Xiyu Formation conglomerates along a subhorizontal fault plane [*Li et al*., 2012].

We observed growth strata within the Xiyu conglomerate at two sites within the Bieertuokuoyi piggyback basin (Figures 3, 4c, 4d, 4f, and 4g). As previously mentioned, at the base of the Bieertuokuoyi Basin, an erosional unconformity separates the underlying Wuqia Group and the overlying Xiyu Formation (N_{x1}) (Figures 3 and 4d). Growth strata occur within the lower Xiyu Formation ~500 m of section above the basal unconformity, as evidenced by minor angular unconformities, wedge-shaped beds, and fanning dips (Figures 4d and 4g). At the top of the piggyback basin section, the second set of Xiyu growth strata can be traced from exposures in the center of the basin southward to where they overlie the TT (Figure 4c).

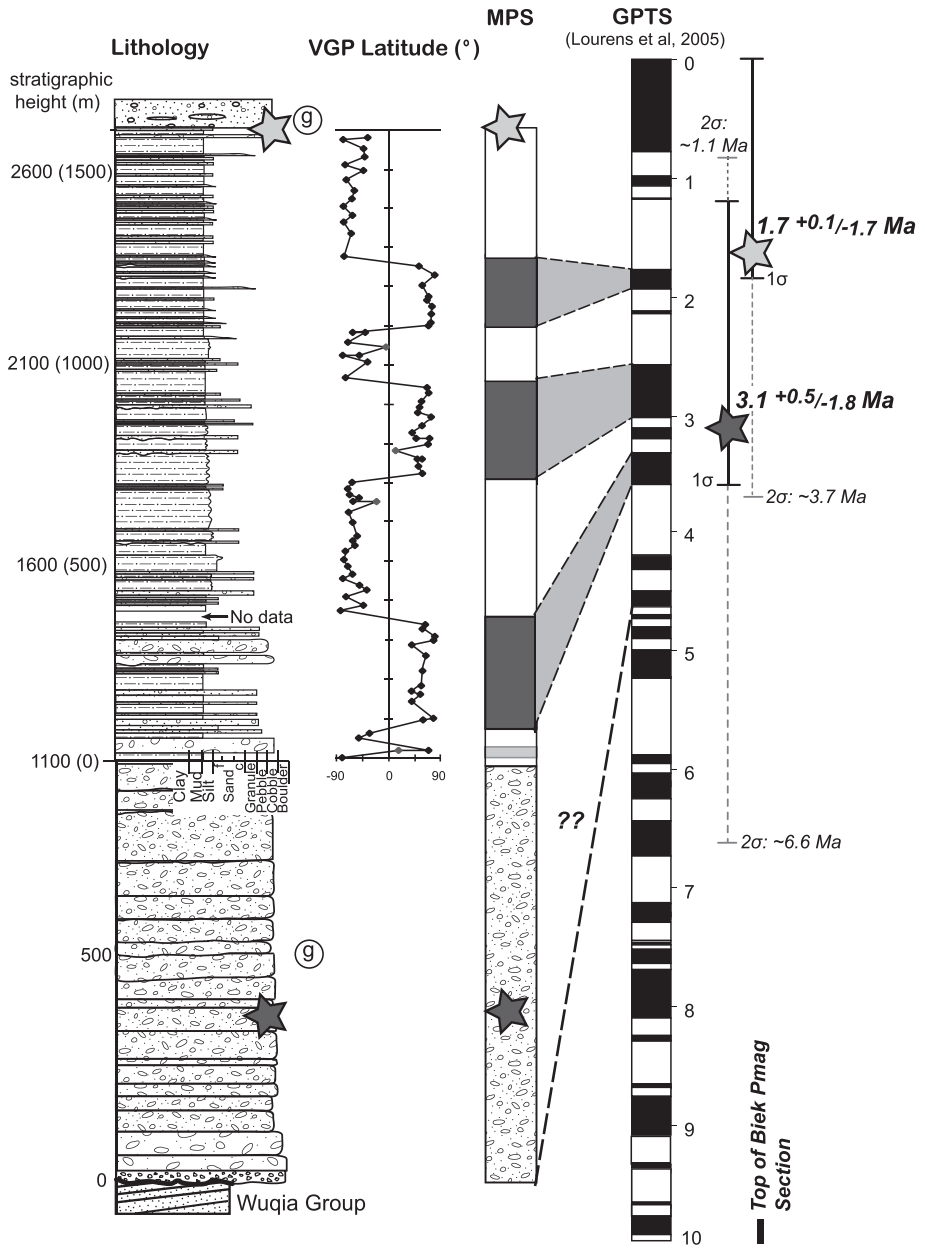

Figure 6. Correlation of our section to the geomagnetic polarity time scale (GPTS) [*Lourens et al.*, 2005]. MPS—Magnetic polarity stratigraphy. VGP latitudes <30° are shown in gray and were not included in determining magnetozones. Stars mark location of cosmogenic burial samples within the stratigraphic and magnetostratigraphic sections, and the circled g marks the stratigraphic locations of growth strata. Black solid lines and dashed grey lines are the 1σ and 2σ errors on the burial samples, respectively. Stratigraphic height refers to the measured height within the section, with heights in parentheses representing height within the sampled magnetostratigraphic section.

5. Magnetostratigraphy

5.1. Magnetostratigraphic Results

We collected two to four specimens at 83 sites for paleomagnetic analysis through a 1.6 km thick, measured section of interbedded fluvial siltstone, sandstone, and conglomerate in the Bieertuokuoyi piggyback basin. Average sample spacing was ~20 m but varied from 1 to 50 m. Detailed methods and results of the magnetostratigraphic analysis can be found in the supporting information. Alternating field and thermal demagnetization procedures clearly resolved a low-coercivity, low-temperature component (LTC), and a high-temperature component (HTC) (Figures 5a–5d). The HTC was determined to be the characteristic

remanent magnetization (ChRM), carried by magnetite and hematite (Figures 5e and 5f), and was used to determine the virtual geomagnetic pole (VGP) latitudes. As in nearly all Neogene sediments in the western Tarim Basin, magnetite and hematite are the dominant magnetic carriers [*Chen et al*., 2002, 2007; *Heermance et al*., 2007].

We used the reversal test to determine if the ChRM had been isolated (Figure S2). The section passes the reversal test with a C quality [*McFadden and McElhinny*, 1990]. A low-quality reversal test can be caused by an unremoved overprint [*McElhinny*, 1964; *Charreau et al*., 2005] that can steepen or flatten the normal polarity directions with respect to the reversed polarity directions. Such an overprint has been observed in nearby Mio-Pliocene magnetostratigraphic studies [i.e., *Chen et al*., 2002; *Heermance et al*., 2007].

We also performed a fold test to determine if the ChRM was acquired during deposition and prior to deformation [*McFadden and Jones*, 1981]. Although the entire magnetostratigraphic section fails a fold test due to the presence of a relatively uniform dip, a subset of 15 high-quality specimens spanning the complete range of dips passes the fold test, suggesting maximum unfolding around 100% (see supporting information Figure S3) [*McFadden and Reid*, 1982; *Watson and Enkin*, 1993; *Enkin and Watson*, 1996].

Given that the section passes the reversal and fold tests and that all normal and reversed polarity directions are qualitatively antipodal, we accept the polarity determinations for the magnetostratigraphic section.

5.2. Uncertainties in the Correlation to the Geomagnetic Polarity Timescale

Based on the VGP latitudes, a magnetic polarity stratigraphy for our section (Figure 6) contains three normal magnetozones and four reversed magnetozones, with each magnetozone defined by at least two sites with the same polarity and a VGP latitude $>30°$. The brevity of the section and low number of reversals precludes unambiguous correlation to the geomagnetic polarity timescale (GPTS) without additional tie points. Therefore, we use two additional constraints to help pin our section to the GPTS. (1) We previously collected a nearby, unpublished 8 km thick magnetostratigraphic section through the Bieertuokuoyi water gap (see Figure 2 for location), spanning the base of the Tertiary through part of the Neogene. The top of this unpublished section lies stratigraphically below the rocks in the piggyback basin and is correlated to around 10 Ma, thus providing an older limit on the age of our section. (2) The top of our section is a reversed magnetozone; and thus, the section must be older than the Brunhes-Matayuma boundary at 0.78 Ma [*Lourens et al*., 2005]. Despite these first two constraints, the section can be correlated to numerous intervals within the remaining span of 1–9 Ma. To help provide further control, a statistical assessment (83 sites, 7 reversals discovered; see supporting information) suggests our section should span 1.7 ± 0.6 Myr [*Johnson and McGee*, 1983] yet still leaves a number of possible correlations.

5.2.1. Burial Ages

To provide independent age control, we collected two $^{26}Al/^{10}Be$ cosmogenic radionuclide burial samples [*Granger and Muzikar*, 2001] from deeply shielded sites containing coarse sand lenses within the Xiyu Formation conglomerates above and below the magnetostratigraphic section. Cosmogenic radionuclide burial dating, which relies on the decay of multiple in situ cosmogenic radionuclides, is emerging as a way to date sediments that range in age from 0.3 to 6 Ma [e.g., *Granger et al*., 1997; *Wolkowinsky and Granger*, 2004; *Balco and Rovey*, 2010; *Craddock et al*., 2010; *Vermeesch et al*., 2010; *Kong et al*., 2011]. The isotopes are produced in quartz as rocks exhume and erode on the hill slopes. Assuming relatively fast exhumation, transport, and burial, the ratio of $^{26}Al/^{10}Be$ at the time of burial is similar to the ratio of their production rates, and any measurable change in that ratio can be interpreted as the time elapsed since burial. Ideally, the sediment to be dated underwent a simple exposure history: it was eroded from a source area where it had accumulated a concentration of ^{10}Be and ^{26}Al in quartz as it was exhumed on the hill slopes; it was transported almost instantaneously (relative to the burial time), deposited, then rapidly buried to a sufficient depth (>30 m) where postburial production effectively stops, and was exhumed shortly before sampling. Unfortunately, a simple transport, burial, and exhumation history, and the assumption that the sample has remained well shielded since its final deposition, are commonly difficult to prove. Both postburial production and a prolonged transport history can have a significant effect on burial ages by increasing the concentration (and hence ratio) of ^{10}Be and ^{26}Al and thus creating apparent younger ages.

At the top of the section, we sampled (PBB-2) a cave ~1 m tall and ~2 m deep within a broader opening ~46 m high and ~14 m deep along tall cliffs of Xiyu Formation (N_{x2}). The cliff face itself is >100 m thick. Large blocks

Table 3. Cosmogenic Burial Data and Ages

Sample No.	Latitude/ Longitude	Elevation (m)	Depth[a] (m)	Mass Qtz (g)	$^{10}Be/^{9}Be$ (10^{-14})[b,c]	^{9}Be Carrier (mg)	[^{10}Be] (10^{4} Atoms g^{-1})	$^{26}Al/^{27}Al$ (10^{-14})[d,e]	^{27}Al (mg)[f]	[^{26}Al] (10^{4} atoms g^{-1})	$^{26}Al/^{10}Be$ Ratio	Age (Ma)[g]
PBB-1	39.5290°N/ 74.8370°E	2589	>50	116.0	7.6 ± 0.6	0.230	1.00 ± 0.08	0.8 ± 0.6	10.25	1.6 ± 1.2	1.6 ± 1.0	$3.1^{+0.5}/_{-1.8}$
PBB-2	39.4921°N/ 74.8515°E	2695	>100	144.7	12.5 ± 0.4	0.220	1.27 ± 0.04	0.4 ± 1.2	21.52	3.3 ± 1.7	2.6 ± 0.8	$1.7^{+0.1}/_{-0.7}$

[a]Depth is the thickness of the overlaying sediment deposits.
[b]Isotope ratios were normalized to ^{10}Be standards prepared by *Nishizumi et al.* [2007] with a value of 2.85×10^{12} and a ^{10}Be half-life of 1.38×10^{6} years [*Chmeleff et al.*, 2010].
[c]$^{10}Be/^{9}Be$ ratios were corrected using a ^{10}Be laboratory blank ($n = 2$) of 9.15×10^{-15} for sample PBB-2 and 9.73×10^{-15} for sample PBB-1.
[d]Isotope ratios were normalized to ^{26}Al standards prepared by *Nishizumi et al.* [2007] and a ^{26}Al half-life of 0.7×10^{6} years.
[e]$^{26}Al/^{27}Al$ ratios were corrected using a laboratory blank ($n = 2$) of 4.09×10^{-15}.
[f]^{27}Al measurements were made using an inductively coupled plasma atomic emission spectrometry.
[g]Ages calculated following constant depth equations in *Granger and Muzikar* [2001] assuming a simple burial history (see text). Ages have 1 sigma errors.

of Xiyu Formation within the broader opening and at the base of the cliffs suggest ongoing erosion through block collapse. Stratigraphically below (~700 m) and ~2 km NW of the magnetostratigraphic section, we collected a sample (PBB-1) beneath an overhang of ~0.5 m within a narrow, deep (~1.5 m wide, 200+ m deep) slot canyon carved into the Xiyu (N_{x1}).

Burial samples were processed using standard University of California Santa Barbara lab protocols (http://www.geog.ucsb.edu/~bodo/pdf/bookhagen_chemSeparation_UCSB.pdf). The purity of quartz was verified by inductively coupled plasma mass spectrometry measurements of Al, which yielded concentrations of <30 mg in all samples. ^{10}Be and ^{26}Al measurements were made at Lawrence Livermore National Laboratory using the 07KNSTD standard [*Nishiizumi et al.*, 2007].

We calculated the burial ages following the constant depth case in *Granger and Muzikar* [2001, section 4.1] and using Monte Carlo methods to model the errors. We used sea level, high-latitude production rates of 4.96 and 30.2 atoms g^{-1} yr^{-1} for ^{10}Be and ^{26}Al [*Balco et al.*, 2008], respectively, scaled to the sample sites following the scaling scheme of *Lal* [1991] and *Stone* [2000]. We used half-lives of 1.38 Myr and 700,000 years for ^{10}Be and ^{26}Al, respectively [*Chmeleff et al.*, 2010; *Norris et al.*, 1983]. Our calculations and hence burial ages rely on four simplifying assumptions:

1. We assumed a rock density of 2.6 g/cm^3 in all calculations.
2. The production rates are scaled to sea level, high-latitude values using the present-day latitude and elevation of the samples. Because the quartz was eroded from a different location than it was deposited (and probably from a higher elevation, given the proximity to two mountain ranges), this assumption introduces some uncertainties into our calculations. For any given erosion rate, a higher average elevation for the source area catchment will yield a higher incoming preburial concentration of the isotopes, due to altitude/elevation scaling of production rates [*Lal*, 1991]. Importantly, it is the initial *ratio* of ^{26}Al and ^{10}Be in the samples that matter more than the independent production rates of ^{26}Al and ^{10}Be.
3. All uncertainties in the reported burial age reflect only the analytical uncertainties from the accelerator mass spectrometry (AMS) on the concentrations of ^{10}Be and ^{26}Al, and we do not propagate uncertainties in the production rates and mean lives. Nonetheless, production rates may have errors up to 10% [*Balco et al.*, 2008]. In our study, the uncertainties in the production rates and mean lives are small compared to the analytical uncertainties, and therefore, we contend it is reasonable to ignore them.
4. We assume an initial $^{26}Al/^{10}Be$ ratio of ~6:1. Although a complicated transport history may modify this initial ratio, such a history is undocumented here, such that we assume that because of the piggyback basin's proximity to high relief, storage and reworking of the sediments was minimal. Future work, such as sampling of modern river sediments to check the initial $^{26}Al/^{10}Be$ ratio, will be required to test this assumption.

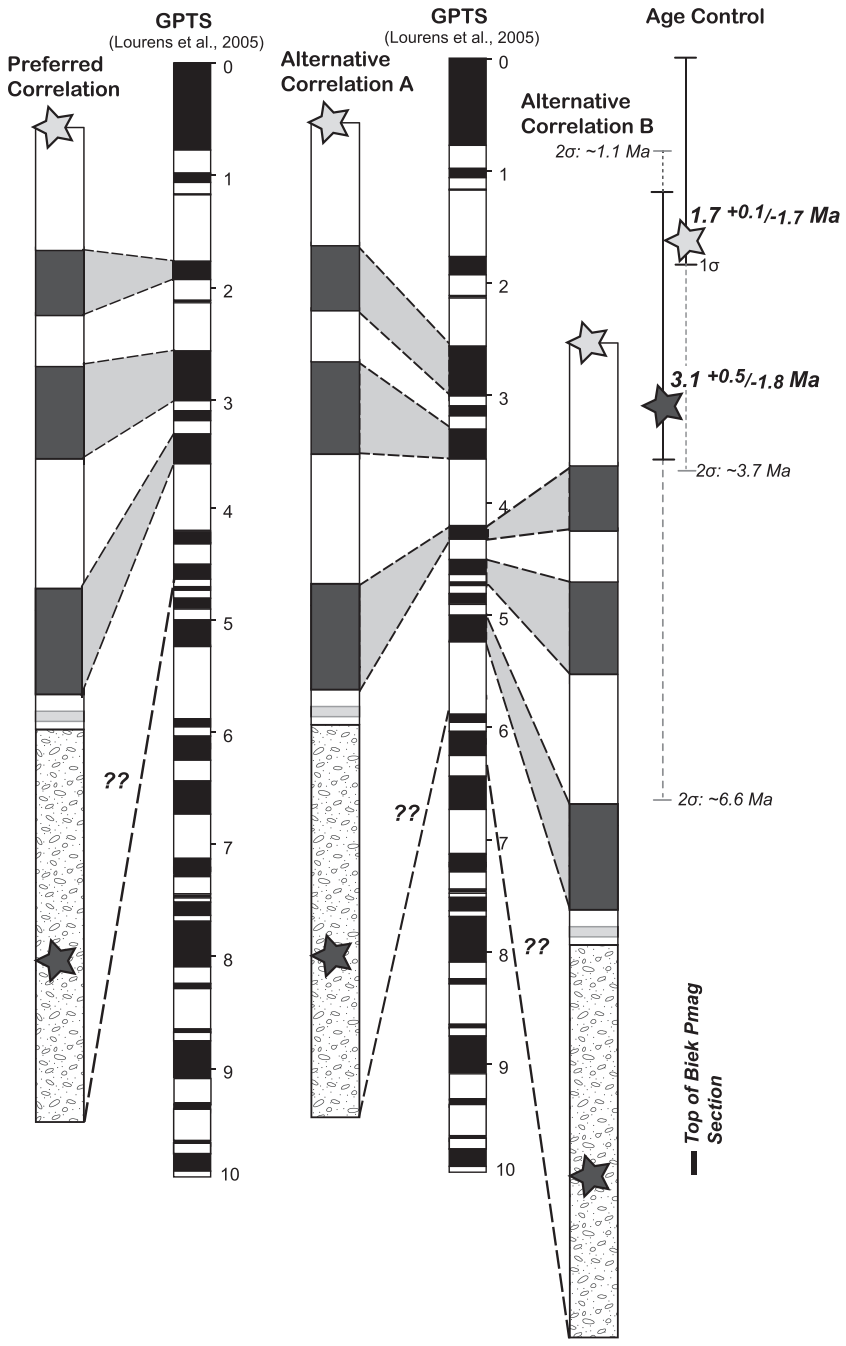

Figure 7. Preferred and two alternative correlations of the magnetostratigraphic section to the GPTS. Stars note locations of burial samples within the magnetostratigraphic section.

The burial age for the Xiyu conglomerate (N_{x1}) near the base of the piggyback basin is 3.1 $^{+0.5}/_{-1.8}$ (1σ) Ma (Figures 6 and S4 and Table 3). The Xiyu conglomerates (N_{x2}) at the top of the basin date to 1.7 $^{+0.1}/_{-1.7}$ (1σ) Ma (Figures 6 and S4 and Table 3). Reported errors are 1σ, but 2σ errors are also used to support our correlation (Figure 6 and Table 3). Importantly, all ages assume postburial and synburial production are negligible. Below, we briefly discuss the uncertainties in our ages due to possible postburial and synburial production.

The sample sites appear to have been well shielded since deposition and only recently exposed due to ongoing uplift and incision of the basin. However, the exact timing of collapse of the cliff face that currently

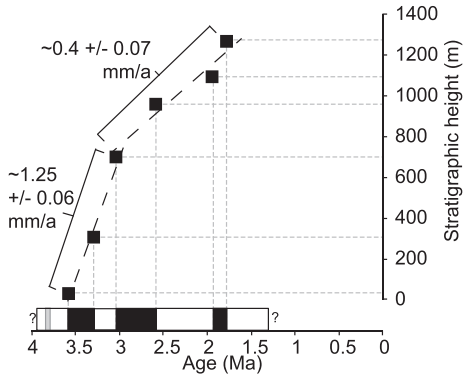

Figure 8. Sediment-accumulation rates within the Bieertuokuoyi piggyback basin. Stratigraphic height refers to the measured height within the magnetostratigraphic section.

shields sample PBB-2 at the top of the section is unknown. Although we assume that recent exposure due to large-scale collapse of the cliff face happened very recently (past few thousand years), the shielding could have been reduced much earlier, causing significant postdepositional production. For example, if the shielding was reduced ~15 ka, the burial age would increase by 5% to ~2.2 Ma [*Thompson*, 2013]. If the shielding was reduced ~100 ka, the burial age would be ~3.3 Ma, an almost 60% increase in age [*Thompson*, 2013]. However, because we currently do not have any additional constraints on when shielding was reduced, we prefer the age reported above of ~1.7 Ma and acknowledge that this is a minimum age. We assume the lower sample, PBB-1, likely has negligible postburial production because of its location within a slot canyon within a thick section of Xiyu Formation.

Synburial production during initial sediment deposition may also perturb the burial ages. In the western Tarim Basin, sediment-accumulation rates of the Xiyu conglomerate are fast enough (400–1100 m/Myr) [*Chen et al*., 2002; *Heermance et al*., 2007; *Li et al*., 2012] (this study) that any correction for syndepositional production during accumulation of the Xiyu is dwarfed by the uncertainty in the burial age [*Craddock et al*., 2010; *Thompson*, 2013]. Hence, we do not account for synburial production in our burial ages. However, we acknowledge that our ages represent apparent minimum ages, as any production of ^{10}Be and ^{26}Al during deposition would lead to an apparent younger burial age due to higher concentrations and, hence, a higher ^{26}Al/^{10}Be ratio.

Despite large errors that are likely due to sample impurities resulting in low currents on the AMS measurements and high stable ^{27}Al concentrations, our two burial samples are in stratigraphic order, only overlap by ~0.6 Myr (using 1 sigma errors), and provide two additional constraints with which to pin our magnetostratigraphic section.

5.3. Correlation to the GPTS

We correlate the magnetostratigraphic section to ~1.5 to ~3.6 Ma (Figure 6), spanning ~1.9 Myr. This correlation matches the expected time span of 1.7 ± 0.6 Myr [*Johnson and McGee*, 1983]. The base of the magnetostratigraphic section, at ~3.6 Ma, lies at the 1 sigma boundary for lower sample PBB-1. Expanding to the 2σ error (3.1 $^{+3.5}/_{-2.0}$ Myr for PBB-1, 1.7 $^{+2.0}/_{-1.7}$ Myr for PBB-2, Figure 6) permits our preferred correlation. The burial age for sample PBB-1 at the base of the section is younger than predicted by our correlation and may be due to incorrect assumptions about the sediment transport and burial history or postburial production. A more complicated or slower burial history or significant amount of postburial production during Quaternary exhumation would create an apparent younger age, thereby implying that the actual depositional age of the sediment may be older. Thus, we conclude our preferred correlation to the GPTS is plausible, despite only encompassing the predicted age of the base of the section by expanding to the 2σ error.

Our preferred magnetostratigraphic correlation to the GPTS (Figure 6) requires that we missed two subchrons. Perhaps our sample spacing was too large to capture every subchron or our sampling spans an unrecognized disconformity (Figure 6). (1) The Reunion subchron, at 2.14–2.15 Ma [*Lourens et al*., 2005] is commonly missed because it spans only 0.01 Myr. In our sampling scheme, the Reunion is shorter than what we would likely capture (~0.03–0.1 Myr with an average sample spacing of 20 m, see supporting information). (2) The normal subchron during the Gauss between 3.11 and 3.21 Ma [*Lourens et al*., 2005] spans 0.1 Myr, which is approximately equal to what our sample spacing would, on average, capture but is short enough that it could also be missed with our spacing. The uncorrelated GPTS chrons could also be due to short depositional hiatuses that we did not recognize in the field or to missing section due to sampling errors in the field.

We also present two alternative (and older) correlations of our magnetostratigraphic section to the GPTS (Figure 7). Both alternative correlations are consistent with the burial ages up to their maximum 2σ error and are younger than the stratigraphically lower Bieertuokuoyi magnetostratigraphic section (Figure 2). However, we prefer the youngest correlation for the following reasons: (1) Alternative correlation A requires that we either did not sample or did not capture one longer subchron (3.11 to 3.21 Ma). Although a single data point at ~1100 m stratigraphic height may be suggestive of a polarity reversal at 3.11 to 3.21 Ma, we should have captured the subchron given our sample spacing and average sediment-accumulation rates in the region (200–1100 m/Myr [*Chen et al*., 2002, 2007; *Sun et al*., 2004; *Charreau et al*., 2006; *Huang et al*., 2006; *Heermance et al*., 2007; *Li et al*., 2012]). With the exception of the lowermost normal magnetozone correlated to the subchron at 4.3 to 4.5 Ma, which requires unrealistically high (~2000 m/Myr) sediment-accumulation rates, alternative correlation A implies sediment-accumulation rates similar to those found in the western Tarim Basin. Alternatively, if we impose a more reasonable sediment-accumulation rate, then the correlation implies we missed another subchron at 4.3 to 4.5 Ma. Thus, we believe alternative correlation A provides a reasonable alternative correlation with the exception of missing one (or maybe two) subchrons. (2) Alternative correlation B requires that we did not sample or did not capture two short subchrons during the Gilbert (4.63 to 4.8 and 4.9 to 5 Ma). Several data points have lower VGP latitudes that may suggest we sampled near a polarity reversal, but we find it unlikely that we would have missed two normal subchrons within the densely sampled intervals between 400 and 600 m. Furthermore, alternative correlation B would require not only rapid, sudden changes in sediment-accumulation rates but also rates that are much higher (1400–1900 m/Myr during some intervals) than any previously published studies. Thus, we believe alternative correlation B is less robust than our preferred correlation and alternative correlation A.

Despite missing two subchrons in the magnetostratigraphic section, we will, henceforth, rely on our preferred correlation to the GPTS, which is a correlation bolstered by the cosmogenic burial ages. Moreover, either our preferred correlation or the alternative correlations indicate that the piggyback basin sediments are likely late Miocene to Pleistocene in age (Figure 7) and provide a first-order age control.

6. Discussion

The Bieertuokuoyi piggyback basin provides a late Miocene-Pleistocene record of deposition and uplift on the northeastern margin of the Pamir Plateau. The magnetostratigraphy, combined with cosmogenic burial ages, provides a likely correlation of the section to the GPTS (Figure 6). Notably, this section is currently the only record of deformation for several structures on the NE Pamir margin. We discuss the controls on deposition in the basin and summarize the stratigraphic and magnetostratigraphic data, as well as field observations and structural mapping in the area, to determine the onset of deformation of the Pamir Frontal Thrust (PFT) and of strands (>3) of the Takegai Thrust (TT) and Kenenbieerte Thrust (KT) on the NE Pamir margin. Finally, we discuss the implications for the tectonic evolution of the NE Pamir margin and the Pamir-Tian Shan collision.

6.1. Stratigraphic Changes Within the Bieertuokuoyi Piggyback Basin: Tectonic Versus Climatic Controls

Grain size changes and accumulation rates within a basin depend on whether the deposition is controlled primarily by subsidence or supply [*Heller and Paola*, 1992; *Paola et al*., 1992]. Typically, progradation of conglomerates in a supply-driven basin coincide with fast subsidence rates and/or faster sediment-accumulation rates. An increase in supply can result from climatic changes or tectonic uplift in the source area. In a subsidence-driven basin, progradation of conglomerates coincides with slower subsidence and sediment-accumulation rates. Subsidence-driven progradation typically occurs during periods of relative tectonic quiescence when erosion is outpacing crustal thickening in bounding mountain ranges.

Sediment-accumulation rate and grain size changes within the Bieertuokuoyi Basin are roughly positively correlated: slower sediment-accumulation rates (~400 m/Myr), correspond to the generally finer grained sediments in the top and middle of the basin, whereas threefold higher sediment-accumulation rates (~1250 m/Myr) correspond to conglomerates and interbedded sandstones at the base (Figure 8). These observations suggest the Bieertuokuoyi Basin is a supply-driven basin in which progradation and retrogradation

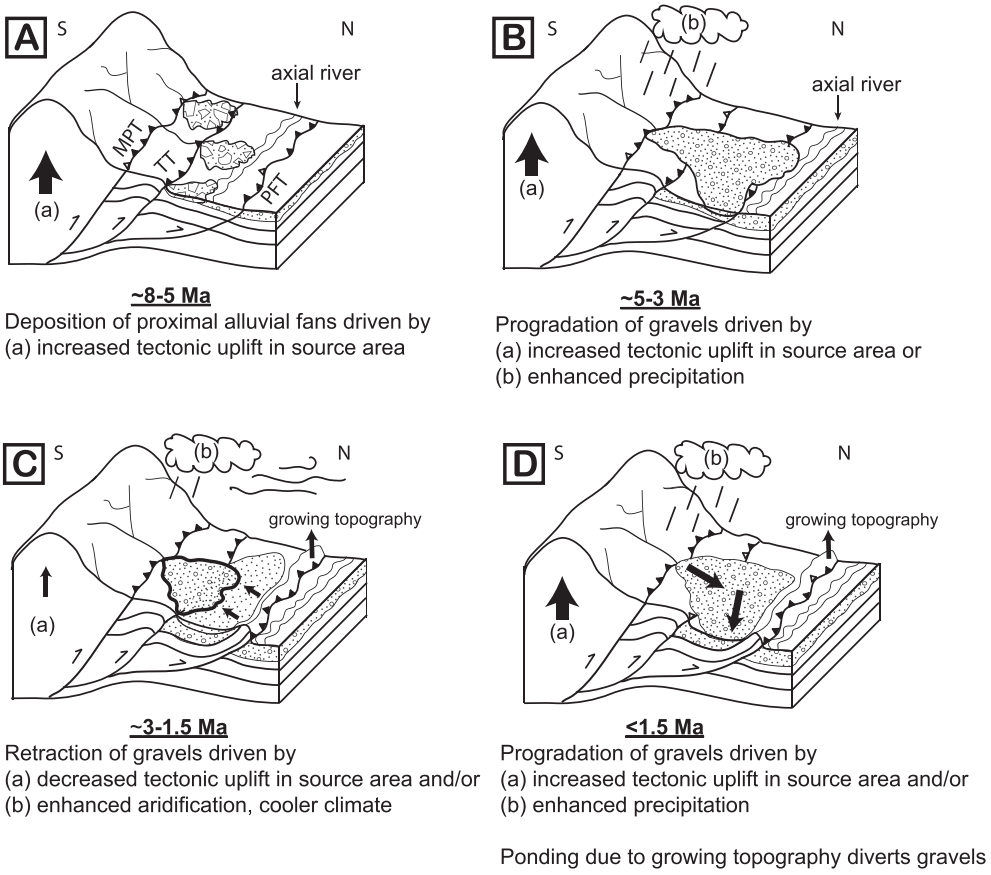

Figure 9. Schematic illustrations of the controls on deposition in the Bieertuokuoyi basin, under the assumption that gravel progradation is supply driven. (a) Local uplift on nearby faults creates proximal alluvial fan deposits, interfingering with a braided axial river. MPT: Main Pamir Thrust; PFT: Pamir Frontal Thrust; TT: Takegai Thrust. (b) Increased rock uplift in the Pamir or enhanced precipitation drives progradation of the Xiyu conglomerates and coeval beveling of growing topography along the Pamir Frontal Thrust and Takegai Thrust in the foreland. (c) Retraction of the gravel front due to either decreased rock uplift in the source area or enhanced aridification and less discharge. Lower discharge/uplift would lower the sediment supply/caliber and inhibit progradation. Growing hanging wall topography ponds finer-grained sediments. (d) Renewed gravel progradation driven by either increased rock uplift in the Pamir or enhanced glacial erosion. Emergent topography diverts gravels toward the Tarim Basin to the east. (e) ASTER scene showing ancient (Bieertuokuoyi, outlined in black) and modern (outlined in grey) piggyback basins on the NE Pamir. Sediment is ponding and partially diverted around growing topography above the Pamir Frontal Thrust. Black arrows indicate general direction of present-day major rivers draining NE Pamir.

of the gravel front was driven by supply changes within the source area. Nearby sites along the NE Pamir margin [*Chen et al.*, 2005; *Li et al.*, 2012] show very rapid (740 ~ 1100 m/Myr) sediment-accumulation rates for the conglomerates as well, supporting the idea that gravel progradation is supply-driven along the NE Pamir. Furthermore, we interpret stratigraphic changes within the piggyback basin section to indicate a change from

proximal alluvial fan deposits to a distal braidplain system before returning to a coarser braided river facies. This succession supports an initial progradation of the gravel front, a subsequent retraction of the front, and then a final progradation.

Below we explore the available data for the region to illuminate possible primary controls on sediment deposition in the Bieertuokuoyi piggyback basin and argue that it is likely driven by both tectonics and climate. In the northeastern Pamir, extensive low-temperature thermochronologic data sets date the onset of exhumation in some of the Bieertuokuoyi basin source areas. Along the NE Pamir extensional domes, exhumation began ~5–6 Ma (Figure 1a) [*Cao et al*., 2013a] or ~7–8 Ma [*Robinson et al*., 2004] and could have driven the initial progradation of Xiyu conglomerate at the base of the basin (N_{x1}) by increasing the sediment supply to the basin through erosion (Figures 9a and 9b). High stream power and/or sediment supply would allow the Xiyu Formation to prograde farther into the basin by beveling the growing topography above the active PFT and TT (Figure 9b).

Retraction of the gravel front, leading to fine-grained deposition within the basin between ~3.0 and ~1.5 Ma (Figure 9c), may be tectonic or climatic in origin. Intensification of Northern Hemisphere glaciations around ~2.5–3 Ma may have increased fluvial and glacial erosion [*Raymo*, 1994; *Zachos et al*., 2001; *Zhang et al*., 2001; *Molnar*, 2004; *Willenbring and von Blanckenburg*, 2010; *Herman et al*., 2013]. Although increased erosion would have increased the sediment supply, a colder, drier climate and aridification after ~3.6 Ma and ~2.6 Ma [*Lu et al*., 2010] may have decreased the discharge and reduced the ability of the rivers to transport large amounts of coarse sediment, thereby inhibiting progradation of the gravel front (Figure 9c). Available thermochronologic data are equivocal and support ongoing exhumation during the Pliocene (Figure 1b) [*Cao et al*., 2013a, 2013b; *Thiede et al*., 2013; *Sobel et al*., 2013], but not necessarily a decrease in exhumation rates. Regardless, a reduction in sediment supply to the basin likely means that rivers draining the NE Pamir into the Bieertuokuoyi basin provided insufficient sediment to the basin to keep pace with the growing topography in the foreland, such that emergent topography above the active Pamir Frontal Thrust began to pond fine-grained sediment within the piggyback basin (Figure 9).

Final progradation of the Xiyu conglomerate at ~1.5 Ma may have been a response to increased exhumation in the NE Pamir (Figure 9d). Recent thermochronologic data sets [*Arnaud et al*., 1993; *Cao et al*., 2013a, 2013b] argue for increased exhumation of the NE Pamir extensional domes since ~2 Ma. Alternatively, possible thrusting along the Oytag fault, a southern splay of the Main Pamir Thrust, around ~3.7 Ma (defined by a single questionable zircon (U-Th)/He age, *Sobel et al*. [2013]) may also have driven tectonically controlled sediment supply in the region. However, despite progradation of the gravel front, possible increased stream power, and sediment supply, the topography above the PFT likely diverted the sediment eastward toward the Tarim Basin (Figures 9d and 9e).

In summary, sediment supply to the Bieertuokuoyi basin was likely driven by both tectonics and climate in the source area. During increased hinterland tectonic activity, the Xiyu conglomerate prograded into the basin, whereas during enhanced aridification, the gravel front may have retracted despite ongoing exhumation, leading to steepening of proximal fans and to ponding and deposition of fine-grained sediments within the basin behind emergent topography above the PFT.

The modern piggyback basin in the hanging wall of the PFT farther east along the margin may be an analogue for the ancient Bieertuokuoyi piggyback basin (Figure 9e). Large volumes of gravels from Late Quaternary fanglomerates draining the NE Pamir are diverted eastward toward the Tarim Basin by the growing topography above the PFT. We speculate a similar situation occurred ~1–2 Ma in the Bieertuokuoyi basin.

6.2. Late Miocene to Early Pliocene Initiation of the Pamir Frontal Thrust

Field observations of growth strata, stratigraphic analysis, and magnetostratigraphy of the Bieertuokuoyi basin sediments support an interpretation that the PFT initiated during the late Miocene to early Pliocene, ~5–6 Ma. Below we summarize these data:

1. The presence of a high-relief erosional unconformity at the base of the Bieertuokuoyi basin (Figures 3 and 4d) dictates at least some uplift and erosion of the Wuqia Group occurred prior to deposition of the Xiyu Formation. Uplift of the Wuqia Group along the PFT would provide locally high relief, and the similarity of clast composition between the alluvial fan clasts and the Wuqia Group strongly supports a local source area. Alternatively, uplift along the Takegai Thrust fault zone to the south (Figures 2 and 4),

with similar Wuqia Group sandstones and siltstones in the hanging wall, could also be a local source for the proximal alluvial fan deposits.

2. The Wuqia Group and underlying Kashi Group precede growth strata. The presence of growth strata within the lower Xiyu Formation (Facies B, N_{x1}) and the upper Xiyu Formation (Facies B, N_{x2}: Figure 2) near the piggyback basin's margins also indicates that the PFT was active during the deposition of the Xiyu Formation (Figures 4f and 4g). We observe minor angular unconformities, fanning dips, and thickening beds.
3. Subsequent stratigraphic changes within the piggyback basin section suggest a change from proximal alluvial fan deposition to a distal braidplain. We interpret the thick, finer grained Plio-Pleistocene sedimentary section above the erosional unconformity and in the hanging wall of the Pamir Frontal Thrust as aggradation and ponding of sediment behind this growing structure. In addition, the rapid (1.25 mm/a) sediment-accumulation rates (Figure 8) of the piggyback basin deposits relative to the size of the basin load supports ponding behind the rising PFT.

Taken together, these stratigraphic and structural data support an interpretation that deposition in the Bieertuokuoyi piggyback basin occurred while the PFT was active. Magnetostratigraphy and cosmogenic burial ages date growth strata near the base of the section to ~4 Ma. However, an additional 500 m of section lies below the burial sample. Extrapolating the relatively uniform sediment-accumulation rate of ~1250 m/Myr through the lower part of the section (Figure 8), in which the same facies dominates (facies B; Figure 3), indicates the very base of the section is at least ~4.5 Ma, and probably closer to 5 Ma. Given an unknown amount of erosion between the initiation of the PFT and subsequent deposition of the piggyback basin, we estimate that uplift on the PFT initiated ~5–6 Ma, during the latest Miocene or early Pliocene.

6.3. Deformation on the Takegai and Kenenbieerte Thrusts

Several episodes of activity are recorded on the Takegai (TT) and Kenenbieerte Thrusts (KT). Based on field observations, we interpret the Kenenbieerte Thrust to have initiated earlier than the Takegai Thrust. Because the folding and faulting observed in the Wuqia Group in the TT hanging wall is not observed in the overlying Xiyu Formation or in the Xiyu Formation in the footwall of the TT (N_{x2}), an earlier deformational event on the Kenenbieerte Thrust (KTa?) or unknown smaller faults to the south of the TT must have occurred prior to local deposition of the Xiyu Formation. The absence of growth strata within the deformed Wuqia Group suggests that this deformation occurred after its Miocene deposition (Table S1) [*Jia et al*., 2004; *Heermance et al*., 2007]. Furthermore, although we lack an exact age constraint on the vertically dipping beds of the Xiyu Formation in the footwall of the TT (Figure 4b), we interpret them as correlative to the Xiyu Formation (N_{x1}) at the base of the piggyback basin. Thus, this deformational episode on a strand of the KT or unknown fault must be older than ~4 Ma. In addition, a splay of the Kenenbieerte Thrust (KTb) places the Eo-Oligocene Bashibulake Formation over the Miocene Wuqia Group and must have initiated after the deposition of the Wuqia Group. Therefore, based on our field observations, we interpret the onset of deformation on the KT to be in the middle or late Miocene, but could be as young as the Mio-Pliocene boundary.

Deformation on the Takegai Thrust (TT) is clearly recorded by the Xiyu Formation at the top of the Bieertuokuoyi basin magnetostratigraphic section (N_{x2}: Figure 2). There, growth strata in the conglomerates can be traced to the south into the hanging wall of the TT, where they rest above an angular unconformity with the Wuqia Group (Figure 4e). This correlation allows us to date the younger Xiyu Formation (N_{x2}) above the TT to ~1.5 Ma. These data indicate that at least the northernmost Takegai fault may have been active synchronously with the Pamir Frontal Thrust beginning around the Mio-Pliocene boundary and continuing until at least 1.5 Ma.

6.4. Implications for the Tectonic Evolution of the NE Pamir Margin

To date, little is known about the timing of thrusting and the northward propagation of the NE Pamir margin. Recent data sets provide considerable age information on the timing of the Kongur Shan Extensional System, the Kashgar-Yecheng Transfer System, and extensional domes within the Pamir plateau (Figure 1b) [*Robinson et al*., 2004; *Sobel et al*., 2011, 2013; *Thiede et al*., 2013; *Cao et al*., 2013a, 2013b]. Below we discuss the current data available for deformation on the NE Pamir margin, place our data into this context, and conclude that our data support a regional shift in the kinematics of deformation at the end of the Miocene [*Chen et al*., 2011].

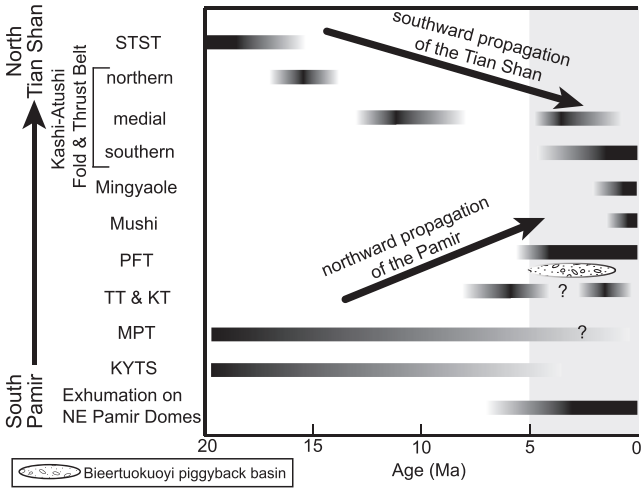

Figure 10. Summary of the timing of deformation of major structures in the Pamir-Tian Shan-Tarim Basin area. Black boxes indicate duration of deformation on structures, and stippled oval shows duration of deposition within the Bieertuokuoyi piggyback basin. Gray bar marks complex sequencing of deformation on structures at the start of the Pliocene. Kashi fold-and-thrust belt is divided into three deformation intervals, following *Heermance et al.* [2008] and includes the following structures: southern—Atushi, Kashi, and Keketamu anticlines; medial—Tashipishake anticline; northern—Kashi Basin Thrust and imbricates. KT—Kenenbieerte Thrust, KYTS—Kashgar-Yecheng Transfer System, MPT—Main Pamir Thrust, PFT—Pamir Frontal Thrust, STST—South Tian Shan Fault, and TT—Takegai Thrust.

6.4.1. Oligocene-Miocene

Widespread late Oligocene to early Miocene contractional features are observed within the Pamir and on its margins [*Sobel and Dumitru*, 1997; *Bershaw et al*., 2012; *Cao et al*., 2013b], marking the onset of larger-scale shortening within the northern Pamir. Thrusting along the Main Pamir Thrust (MPT) initiated in either the late Oligocene [*Yin et al*., 2002] or early Miocene [*Sobel and Dumitru*, 1997] and was likely well underway by ~20 Ma [*Sobel and Dumitru*, 1997; *Bershaw et al*., 2012] based on apatite fission track, magnetostratigraphy, and detrital zircon ages. Near the southern end of our study area, we deduce that thrusting on the MPT began around the same time, although unreset Mesozoic apatite fission track and zircon (U-Th)/He ages in the hanging wall of the MPT (Figure 1b) [*Sobel et al*., 2013] suggest that little exhumation (<7 km) of the hanging wall of the MPT occurred during the Miocene. Basin-vergent thrusting to the south along the Tiklik fault (not shown in Figure 1a, to southeast of the Kashgar-Yecheng Transfer System) [*Wang et al*., 2003] and transpression along the Kumtag fault, a branch of the Kashgar-Yecheng Transfer System (Figure 1a) [*Sobel and Dumitru*, 1997; *Cao et al*., 2013b] also support widespread shortening along the Pamir's margins. In addition, initiation of orogen-wide exhumation in the Central Pamir began 21–13 Ma [*Lukens et al*., 2012] or after ~20 Ma [*Stearns et al*., 2013]. Shortening may also have been translated across the Tarim plate to the southern Tian Shan, where reactivation of major thrust faults on the southern margin began ~20 Ma [*Sobel et al*., 2006; *Heermance et al*., 2008].

6.4.2. Late Miocene-Quaternary

The NE Pamir underwent a second pulse of tectonic activity that initiated in the late Miocene or early Pliocene, as recorded in the Bieertuokuoyi basin stratigraphy and structures (Figure 10). Our initiation age of ~5–6 Ma on the Pamir Frontal Thrust is consistent with other segments along strike. *Fu et al*. [2010] estimated the initiation age of the easternmost PFT, near Oytag, to be ~3.5 Ma, based on extrapolation of a long-term slip rate and large-scale measured offsets. In the Alai Valley in Kyrgyzstan, along the northern margin of the Pamir, the westward extension of the PFT (called the Main Pamir Thrust in that locality) initiated 4–6 Ma [*Arrowsmith and Strecker*, 1999]. Along the northwestern margin of the Pamir, thrusting initiated during the late Miocene to Pliocene [*Pavlis et al*., 1997].

Deformation on the Takegai Thrust may have been synchronous with the PFT (4–6 Ma) but could be as young as ~2 Ma, and shortening continued until at least ~1.5 Ma. Despite intense deformation of the Wuqia Group in the Takegai Thrust hanging wall, the presence of undeformed Xiyu Formation unconformably above the Wuqia Group, clearly suggests pulsed deformation on the Takegai/Kenenbieerte Thrust zone. Therefore, deformation on the NE Pamir front did not step persistently outward, but rather Plio-Pleistocene deformation was distributed between both the Takegai Thrust and PFT until recently. Moreover, a single 3.7 Ma zircon (U-Th)/He age near the MPT [*Sobel et al*., 2013], a new cosmogenic burial age of ~3.3 Ma from possible growth strata related to the MPT [*Thompson*, 2013], and field observations of growth strata within an alluvial fan overlying the ~3.3 Ma strata suggest active shortening on the Main Pamir Thrust to the south. Hence, active deformation was distributed across the outer 40 km of the Pamir's NE margin until the Quaternary.

Furthermore, numerous geochronologic data sets suggest a shift in the regional deformation patterns at the end of the Miocene into the early Pliocene [*Chen et al*., 2011; *Sobel et al*., 2011]. The Kashgar-Yecheng Transfer system (KYTS) has slowed since 3–5 Ma, based on thermochronologic data across the KYTS fault system [*Sobel et al*., 2011]. The decrease in the slip rate of this large strike-slip system of the eastern margin of the Pamir is interpreted to reflect an increase in the northward velocity of the Tarim, suggesting increased coupling of the Tarim and Pamir domains, rather than a slow-down of the Pamir [*Sobel et al*., 2011]. Moreover, recent GPS data indicate little shortening now occurs along the eastern margin of the Pamir [*Ischuk et al*., 2013], despite the abundant shortening structures that were active during the Paleogene and Miocene [*Yin et al*., 2002; *Bershaw et al*., 2012]. In fact, an increase in deformation and southward migration of the Tian Shan Kashi-Atushi fold-and-thrust belt suggests the transfer of shortening across the relatively rigid Tarim Basin block into the southern Tian Shan around the same time (~4 Ma) [*Heermance et al*., 2008; *Sobel et al*., 2011]. Exhumation of domes in the northeastern Pamir began 5–8 Ma (Figure 1b) [*Robinson et al*., 2007, 2010; *Thiede et al*., 2013] and continues to the present at fast rates (~2–5 mm/a) [*Robinson et al*., 2007; *Thiede et al*., 2013; *Cao et al*., 2013a, 2013b; *Sobel et al*., 2013].

North directed paleocurrents and changes in clast provenance (Figure 3) within the Bieertuokuoyi piggyback basin are consistent with continued exhumation and uplift of the Pamir to the south during the Pliocene and into the Quaternary. The presence of granitic and metamorphic rocks in the lower basin may represent continued rapid exhumation of the NE Pamir domes to the south of the basin [*Thiede et al*., 2013; *Sobel et al*., 2013], whereas the abundance of limestone clasts in the upper basin are likely from modest exhumation and erosion of Paleozoic limestone along the northern margin of the Pamir. The appearance of abundant limestone clasts at ~2 Ma approximately coincides with the onset of Quaternary glaciations [*Raymo*, 1994] and an increase in exhumation rates on the NE Pamir domes [*Arnaud et al*., 1993; *Cao et al*., 2013a]. Regardless of provenance, the N-S transport direction, coupled with the changes in clast provenance, supports continued exhumation of the NE Pamir margin through the Pliocene and into the Quaternary [*Cao et al*., 2013a; *Sobel et al*., 2013; *Thiede et al*., 2013].

In conjunction with large-scale northward propagation of the thrust faults on the northern margins and the cessation of slip on the Kashgar-Yecheng Transfer System, the onset of E-W extension of the Kongur extensional system in the Pamir was accompanied by the transfer of shortening across the Tarim Basin to the southern Tian Shan and suggests a regional shift in kinematics that led to the another pulse of outward growth of the Pamir ~5–6 Ma [*Chen et al*., 2011]. Increased coupling between the Pamir and Tarim blocks at that time [*Sobel et al*., 2011] would transfer shortening northward to the Pamir frontal faults, in addition to translating shortening across the quasi-rigid Tarim block to the Tian Shan.

6.5. Coeval Thrusting on the NE Pamir Margin

Traditional conceptual models of collisional orogens argue that deformation will step sequentially and unidirectionally toward the foreland as the orogen grows, with slip on hinterland faults ceasing as new faults initiate in the foreland [*Armstrong and Oriel*, 1965; *Dahlstrom*, 1970]. Alternative models suggest that out-of-sequence faulting and deformation in the hinterland are necessary to maintain a critically tapered wedge [*Davis et al*., 1983; *Dahlen*, 1990]. In the southern Tian Shan, pulsed deformation since the early Miocene facilitated southward propagation of the thrust system (Figure 10) [*Heermance et al*., 2008], with modest hinterland deformation, but the majority of the shortening at any given time being accommodated by structures along the frontal edge. Evidence from a Plio-Pleistocene (?) piggyback basin in the hinterland [*Heermance et al*., 2007, 2008] indicates that deformation may have been distributed across the margin intermittently during the late Neogene. Currently, the majority of the deformation along the Tian Shan margin is accommodated on detachment folds along the leading margin, with slow (~1 mm/a) deformation rates on structures in the medial foreland [*Heermance et al*., 2008].

Similarly, the Pamir orogen appears to have coeval thrusting on its frontal faults with deformation distributed across the margin (Figure 10). Although the initiation and duration of thrusting on the MPT is not well constrained, available data suggest the fault was active from ~20 Ma [*Sobel and Dumitru*, 1997; *Bershaw et al*., 2012] possibly into the Quaternary [*Sobel et al*., 2013; *Thompson*, 2013]. Thrusting began on the Takegai and Kenenbieerte thrusts as early as the middle or late Miocene and continued until at least ~1.5 Ma, perhaps synchronous with the MPT. Around ~5–6 Ma, the Pamir deformation front migrated northward to the Pamir Frontal Thrust, synchronous with deformation on the Takegai Thrust (TT). During the Quaternary, the

deformation front may be stepping northward again, manifested as fault-tip and detachment folds in the foreland initiating during the last 1.5 Myr, as significant deformation on the TT ceases [*Chen et al*., 2005; *Li et al*., 2013; *Thompson*, 2013]. In contrast, in the Alai Valley, farther west along the Pamir front (Figure 1a) deformation stepped outward during the Miocene, yet a majority of the Holocene shortening is accommodated on the Main Pamir Thrust, indicating back stepping of deformation onto more hinterland thrusts [*Arrowsmith and Strecker*, 1999].

Furthermore, during the late Quaternary, shortening rates across the NE Pamir margin and NW Tarim Basin have remained relatively constant [*Li et al*., 2012; *Thompson*, 2013], despite being accommodated on different structures. Therefore, coeval thrusting accommodated deformation on the suite of faults along the NE Pamir margin during the Miocene to the present. Distributed deformation across multiple faults and folds, back stepping of the deformation front, and hinterland deformation appear to play important roles in the growth of the Pamir orogen.

7. Conclusions

The Bieertuokuoyi piggyback basin in the hanging wall of the Pamir Frontal Thrust (PFT) provides a clear record of late Cenozoic deformation along the NE Pamir margin. Stratigraphic and magnetostratigraphic data, in combination with field observations and cosmogenic burial ages, show the Bieertuokuoyi basin was formed (and sediments were deposited) after the initiation of the PFT ~5–6 Ma. Additionally, the basin records deformation along strands of the Takegai Thrust (TT) and Kenenbieerte Thrust (KT). At least two episodes of TT/KT deformation have occurred: one in the middle or late Miocene on the KT and a second one synchronous with slip on the PFT and continuing until ~1.5 Ma on the TT. Progradation and retraction of gravels was both climatically and tectonically controlled. Retraction of the gravel front ~3–1.5 Ma occurred in response to ponding behind the emergent growing topography above the PFT. Furthermore, clast provenance and paleocurrent changes throughout the basin record uplift and exhumation of the Pamir to the south [*Robinson et al*., 2004; *Thiede et al*., 2013; *Cao et al*., 2013b; *Sobel et al*., 2013] from the Pliocene to Recent.

The onset of shortening along the Main Pamir Thrust on the NE Pamir margin began in the early Miocene (~20 Ma) [*Sobel and Dumitru*, 1997; *Bershaw et al*., 2012; *Cao et al*., 2013b], and deformation propagated northward to the Takegai Thrust and Pamir Frontal Thrust during the Middle Miocene to Pliocene. Coeval deformation on the Main Pamir Thrust, Kenenbieerte Thrust, Takegai Thrust, and Pamir Frontal Thrust accommodated shortening throughout the Miocene to Recent. In contrast to the more unilateral southward propagation of deformation in the Tian Shan, back-stepping and hinterland deformation appear to play an important role in accommodating shortening along the NE Pamir margin.

Our data suggest a change in the regional kinematics around the Miocene-Pliocene boundary ~5–6 Ma. Rapid exhumation of NE Pamir domes, coupled with cessation of the KYTS, accelerated both a southward propagation of the Kashi fold-and-thrust belt in the Tian Shan and an outward stepping of the northeastern Pamir margin. This synchronous behavior signifies the coupling of the Pamir and Tarim blocks and the transfer of shortening north to the Pamir frontal faults and across the quasi-rigid Tarim Basin to the southern Tian Shan fold-and-thrust system.

Acknowledgments

Magnetostratigraphic data used to create the timescale in Figure 6 are available in Table S2 of the supporting information. Detailed paleomagnetic data of the samples and all other data are available from the authors upon request. U.S. NSF (EAR 1050070), a grant from State Key Laboratory of Earthquake Dynamics of China (LED2010A04), and the International Science and Technology Cooperation Program of China (2008DFA20860) provided funding for this project. J. Thompson was supported by a NSF graduate research fellowship, a NSF East Asia and Pacific Summer Institute (EAPSI) fellowship, and a California Space Grant fellowship. We thank Isaac Jones and Joe Kirschvink for help with the paleomagnetic analysis and Burch Fisher for help in the processing of the cosmogenic samples. Early comments on this manuscript by Aaron Bufe and Ben Melosh greatly improved its focus. Ben Melosh, Xiaodong Yang, Zhaode Yuan, Huili Yang, and Weipeng were a great help in the field. We thank Julien Charreau and one anonymous reviewer for constructive and helpful reviews and AE Taylor Schildgen for constructive comments that significantly improved the manuscript.

References

Amidon, W. H., and S. A. Hynek (2010), Exhumational history of the north central Pamir, *Tectonics*, *29*, TC5017, doi:10.1029/2009TC002589.

Armstrong, F. C., and S. S. Oriel (1965), Tectonic development of Idaho-Wyoming thrust belt, *AAPG Bull.*, *49*, 1847–1866.

Arnaud, N. O., M. Brunel, J. M. Cantagrel, and P. Tapponnier (1993), High cooling and denudation rates at Kongur Shan, Eastern Pamir (Xinjiang, China) revealed by $^{40}Ar/^{39}Ar$ alkali feldspar thermochronology, *Tectonics*, *12*(6), 1335–1346, doi:10.1029/93TC00767.

Arrowsmith, J. R., and M. R. Strecker (1999), Seismotectonic range-front segmentation and mountain-belt growth in the Pamir–Alai region, Kyrgyzstan (India–Eurasia collision zone), *Geol. Soc. Am. Bull.*, *111*, 1665–1683, doi:10.1130/0016-7606(1999)111<1665:SRFSAM>2.3.CO;2.

Balco, G., and C. W. Rovey (2010), Absolute chronology for major Pleistocene advances of the Laurentide Ice Sheet, *Geology*, *38*, 795–798.

Balco, G., J. O. Stone, N. A. Lifton, and T. J. Dunai (2008), A complete and easily accessible means of calculating surface exposure ages or erosion rates form ^{10}Be and ^{26}Al measurements, *Quat. Geochronol.*, *3*, 174–195.

Bershaw, J., C. N. Garzione, L. Schoenbohm, G. Gehrels, and L. Tao (2012), Cenozoic evolution of the Pamir plateau based on stratigraphy, zircon provenance, and stable isotopes of foreland basin sediments at Oytag (Wuyitake) in the Tarim Basin (west China), *J. Asian Earth Sci.*, *44*, 136–148, doi:10.1016/j.jseaes.2011.04.020.

Blair, T. C., and J. G. McPherson (1992), The Trollheim alluvial-fan and facies model revisited, *Geol. Soc. Am. Bull.*, *104*(6), 762–769, doi:10.1130/0016-7606(1992)104<0762:TTAFAF>2.3.CO;2.

Blair, T. C., and J. G. McPherson (1994), Alluvial fans and their natural distinction from rivers based on morphology, hydraulic processes, sedimentary processes, and facies assemblages, *J. Sediment. Res.*, *64*, 450–489.

Burbank, D. W., and R. G. H. Raynolds (1988), Stratigraphic keys to the timing of thrusting in terrestrial foreland basins: Applications to the northwest Himalaya, in *New Perspectives in Basin Analysis*, edited by K. Kleinspehn and C. Paola, pp. 331–352, New York, Springer, doi:10.1007/978-1-4612-3788-4_17.

Burtman, V. S., and P. H. Molnar (1993), Geological and geophysical evidence for deep subduction of continental crust beneath the Pamir, *Geol. Soc. Am. Spec. Pap.*, *281*, 76.

Cao, K., M. Bernet, G. C. Wang, P. van der Beek, A. Wang, K. X. Zhang, and E. Enkelmann (2013a), Focused Pliocene-Quaternary exhumation of the Eastern Pamir dones, western China, *Earth Planet. Sci. Lett.*, *363*, 16–26, doi:10.1016/j.epsl.2012.12.023.

Cao, K., G. C. Wang, P. van der Beek, M. Bernet, and K. X. Zhang (2013b), Cenozoic thermo-tectonic evolution of the northeastern Pamir revealed by zircon and apatite fission-track thermochronology, *Tectonophysics*, *589*, 17–32, doi:10.1016/j.tecto.2012.12.038.

Charreau, J., Y. Chen, S. Gilder, S. Dominguez, J. Avouac, S. Sen, D. J. Sun, Y. A. Li, and M. W. Wang (2005), Magnetostratigraphy and rock magnetism of the Neogene Kuitun He section (northwest China): Implications for late Cenozoic uplift of the Tianshan Mountains, *Earth Planet. Sci. Lett.*, *230*, 177–192, doi:10.1016/j.epsl.2004.11.002.

Charreau, J., S. Gilder, Y. Chen, S. Dominguez, J. Avouac, M. Jovilet, Y. Li, and W. Wang (2006), Magnetostratigraphy of the Yaha Section, Tarim Basin (China): 11 Ma acceleration in erosion and uplift of the Tian Shan mountains, *Geology*, *34*, 181–184, doi:10.1130/G22106.1.

Charreau, J., J. P. Avouac, Y. Chen, S. Dominguez, and S. Gilder (2008), Miocene to present kinematics of fault-bend folding across the Huerguosi anticline, northern Tianshan (China), derived from structural, seismic, and magnetostratigraphic data, *Geology*, *36*, 871–874, doi:10.1130/G25073A.1.

Charreau, J., C. Gumiaux, J. P. Avouac, R. Augier, Y. Chen, L. Barrier, S. Gilder, S. Dominguez, N. Charles, and Q. Wang (2009), The Neogene Xiyu Formation, a diachronous prograding gravel wedge at front of the Tianshan: Climatic and tectonics implications, *Earth Planet. Sci. Lett.*, *287*, 298–310, doi:10.1016/j.epsl.2009.07.035.

Chen, H. L., F. F. Zhang, X. G. Cheng, L. Laio, J. C. Luo, B. Q. Wang, C. F. Yang, and L. F. Chen (2010), The deformation features and basin-range coupling structure in the northeastern Pamir tectonic belt [in Chinese with English abstract], *Chin. J. Geol.*, *45*, 102–112.

Chen, J., G. Qu, X. Feng, and J. Hu (1997), Arcuate thrust tectonics and its contemporary seismicity in the eastern section of the external zone of the Pamir [in Chinese with English abstract], *Seismol. Geol.*, *19*(4), 301–312.

Chen, J., D. W. Burbank, K. M. Scharer, E. Sobel, J. Yin, C. Rubin, and R. Zhao (2002), Magnetostratigraphy of the upper Cenozoic strata in the Southwestern Chinese Tian Shan: Rates of Pleistocene folding and thrusting, *Earth Planet. Sci. Lett.*, *195*, 113–130, doi:10.1016/S0012-821X(01)00579-9.

Chen, J., K. M. Scharer, D. W. Burbank, R. V. Heermance, and C. S. Wang (2005), Quaternary detachment folding of the Mingyaole anticline, southwestern Tian Shan [in Chinese with English abstract], *Seismol. Geol.*, *27*, 530–547.

Chen, J., R. V. Heermance, K. M. Scharer, D. W. Burbank, M. Jijun, and C. S. Wang (2007), Quantification of growth and lateral propagation of the Kashi anticline, SW Chinese Tian Shan, *J. Geophys. Res.*, *112*, B03S16, doi:10.1029/2006JB004345.

Chen, J., T. Li, W. Li, and Z. Yuan (2011), Late Cenozoic and present tectonic deformation in the Pamirs salient, northwestern China [in Chinese with English abstract], *Seismol. Geol.*, *33*(2), 241–259.

Chmeleff, J., F. von Blankenburg, K. Kossert, and D. Jakob (2010), Determination of the 10Be half-life by multicollector ICP-MS and liquid scintillation counting, *Nucl. Instrum. Meth. Phys. Res.*, *268*, 192–199.

Collinson, J. D. (1996), Alluvial sediments, in *Sedimentary Environments: Processes, Facies, and Stratigraphy*, edited by H. G. Reading, pp. 37–82, Blackwell Inc., Oxford.

Coutand, I., M. R. Strecker, J. R. Arrowsmith, G. Hilley, R. C. Thiede, A. Korjenkov, and M. Omuraliev (2002), Late Cenozoic tectonic development of the intramontane Alai Valley, (Pamir-Tien Shan region, central Asia): An example of intracontinental deformation due to the Indo-Eurasia collision, *Tectonics*, *21*(6), 1053, doi:10.1029/2002TC001358.

Craddock, W. H., E. Kirby, N. W. Harkins, H. Zhang, X. Shi, and J. Liu (2010), Rapid fluvial incision along the Yellow River during headward basin integration, *Nat. Geosci.*, *3*, 209–213, doi:10.1038/ngeo777.

Dahlen, F. A. (1990), Critical taper model of fold-and-thrust belts and accretionary wedges, *Annu. Rev. Earth Planet. Sci.*, *18*, 55–99, doi:10.1146/annurev.ea.18.050190.000415.

Dahlstrom, C. D. A. (1970), Structural geology of the eastern margin of the Canadian Rocky Mountains, *Bull. Can. Petrol. Geol.*, *18*, 332–406.

Davis, D., J. Suppe, and F. A. Dahlen (1983), Mechanics of fold-and-thrust belts and accretionary wedges, *J. Geophys. Res.*, *88*, 1153–1172, doi:10.1029/JB088iB02p01153.

DeCelles, P. G., and K. A. Giles (1996), Foreland basin systems, *Basin Res.*, *8*, 105–123, doi:10.1046/j.1365-2117.1996.01491.x.

DeCelles, P., M. B. Gray, K. D. Ridgway, R. B. Cole, P. Srivastava, N. Pequera, and D. A. Pivnik (1991a), Kinematic history of a foreland basin uplift from Paleogene synorogenic conglomerate, Beartooth Range, Wyoming and Montana, *Geol. Soc. Am. Bull.*, *103*, 1458–1475, doi:10.1130/0016-7606(1991)103<1458:KHOAFU>2.3.CO;2.

DeCelles, P., M. B. Gray, K. D. Ridgway, R. B. Cole, D. A. Pivnik, N. Pequera, and P. Srivastava (1991b), Controls on synorogenic alluvial-fan architecture, Beartooth Conglomerate (Palaeocene), Wyoming and Montana, *Sedimentology*, *38*, 567–590, doi:10.1111/j.1365-3091.1991.tb01009.x.

Ducea, M. N., et al. (2003), Building the Pamirs: The view from the underside, *Geology*, *31*(10), 849–852, doi:10.1130/G19707.1.

Enkin, R. J., and G. S. Watson (1996), Statistical analysis of paleomagnetic inclination data, *Geophys. J. Int.*, *126*, 495–504, doi:10.1111/j.1365-246X.1996.tb05305.x.

Fu, B., Y. Ninomiya, and J. Guo (2010), Slip partitioning in the northeast Pamir–Tian Shan convergence zone, *Tectonophys*, *483*, 344–364, doi:10.1016/j.tecto.2009.11.003.

Granger, D. E., and P. F. Muzikar (2001), Dating sediment burial with in situ produced cosmogenic nuclides: Theory, techniques, and limitations, *Earth Planet. Sci. Lett.*, *188*, 269–281, doi:10.1016/S0012-821X(01)00309-0.

Granger, D. E., J. W. Kirchner, and R. C. Finkel (1997), Quaternary downcutting rate of the New River, Virginia, measured from differential decay of cosmogenic 26Al and 10Be in cave-deposited alluvium, *Geology*, *25*(2), 107–110.

Hacker, B., P. Luffi, V. Lutkov, V. Minaev, L. Ratschbacher, T. Plank, M. N. Ducea, A. E. Patiño-Douce, M. McWilliams, and J. Metcalf (2005), Near-ultrahigh pressure processing of continental crust: Miocene crustal xenoliths from the Pamir, *J. Petrol.*, *46*, 1661–1687, doi:10.1093/petrology/egi030.

Heermance, R., J. Chen, D. W. Burbank, and C. S. Wang (2007), Chronology and tectonic controls of Late Tertiary deposition in the southwestern Tian Shan foreland, NW China, *Basin Res.*, *19*, 599–632, doi:10.1111/j.1365-2117.2007.00339.x.

Heermance, R., J. Chen, D. W. Burbank, and J. Miao (2008), Temporal constraints and pulsed Late Cenozoic deformation during structural disruption of the active Kashi foreland, northwest China, *Tectonics*, *27*, TC6012, doi:10.1029/2007TC002226.

Herman, F., D. Seward, D. G. Valla, A. Carter, B. Kohn, S. D. Willett, and T. A. Ehlers (2013), Worldwide acceleration of mountain erosion under a cooling climate, *Nature*, *504*(7480), 423.

Heller, P. L., and C. Paola (1992), The large-scale dynamics of grain-size variation in alluvial basins, 2. Application to syntectonic conglomerate, *Basin Res.*, *4*(2), 91–102.
Huang, B., J. D. A. Piper, S. Peng, T. Liu, Z. Li, Q. Wang, and R. Zhu (2006), Magnetostratigraphic study of the Kuche Depression, Tarim Basin, and Cenozoic uplift of the Tian Shan range, western China, *Earth Planet. Sci. Lett.*, *251*, 346–364, doi:10.1016/j.epsl.2006.09.020.
Hubert-Ferrari, A., J. Suppe, R. Gonzalez-Mieres, and X. Wang (2007), Mechanism of active folding of the landscape (southern Tian Shan, China), *J. Geophys. Res.*, *112*, B03S09, doi:10.1029/2006JB004362.
Ischuk, A., et al. (2013), Kinematics of the Pamir and Hindu Kush regions from GPS geodesy, *J. Geophys. Res. Solid Earth*, *118*, 1–9, doi:10.1002/jgrb.50185.
Jia, C., S. Zhang, and S. Wu (2004), *Stratigraphy of the Tarim Basin and Adjacent Areas* [in Chinese With English Abstract], 1063 pp., Sci. Press, Beijing.
Johnson, N. M., and V. E. Mcgee (1983), Magnetic Polarity Stratigraphy-Stochastic Properties of Data, Sampling Problems, and the Evaluation of Interpretations, *J. Geophys. Res.*, *88*(B2), 1213–1221, doi:10.1029/JB088iB02p01213.
Jones, S. J., L. E. Frostick, and T. R. Astin (2001), Braided stream and flood plain architecture: The Rio Vero Formation, Spanish Pyrenees, *Sediment. Geol.*, *139*, 229–260, doi:10.1016/S0037-0738(00)00165-2.
Jordan, T. E., P. B. Flemings, and J. A. Beer (1988), Dating of thrust belt activity by dating of foreland basin strata, in *New Perspectives in Basin Analysis*, edited by K. Kleinspehn and P. Paola, pp. 307–330, Springer, New York, doi:10.1007/978-1-4612-3788-4_16.
Kong, P., Y. Zheng, and B. Fu (2011), Cosmogenic nuclide burial ages and provenance of Late Cenozoic deposits in the Sichuan Basin: Implications for Early Quaternary glaciations in east Tibet, *Quat. Geochronol.*, *6*, 304–312.
Lal, D. (1991), Cosmic ray labeling of erosion surfaces: In situ nuclide production rates and erosion models, *Earth Planet. Sci. Lett.*, *104*(2), 424–439.
Li, T., J. Chen, J. A. Thompson, D. W. Burbank, and W. Xiao (2012), Equivalency of geologic with geodetic rates in contractional orogens: New insights from the Pamir Frontal Thrust, *Geophys. Res. Lett.*, *39*, L15305, doi:10.1029/2012GL051782.
Li, T., J. Chen, J. A. Thompson, D. W. Burbank, and X. D. Yang (2013), Quantification of three-dimensional folding using fluvial terraces: A case study from the Mushi anticline, northern margin of the Chinese Pamir, *J. Geophys. Res. Solid Earth*, *118*, 4628–4647, doi:10.1002/jgrb.50316.
Limarino, C., A. Tripaldi, S. Marenssi, L. Net, G. Re, and A. Caselli (2001), Tectonic control on the evolution of the fluvial systems of the Vinchina Formation (Miocene), northwestern Argentina, *J. S. Amer. Earth Sci.*, *14*, 751–762, doi:10.1016/S0895-9811(01)00067-0.
Lourens, L. J., F. J. Hilgen, J. Laskar, N. J. Shackelton, and D. Wilson (2005), The Neogene period, in *Geological Time Scale*, edited by F. M. Gradstein et al., pp. 409–440, Cambridge Univ. Press, Cambridge, U. K.
Lu, H., X. Wang, and L. Li (2010), Aeolian sediment evidence that global cooling has driven late Cenozoic stepwise aridification in central Asia, *Geol. Soc. London. Spec. Pub.*, *342*, 29–44, doi:10.1144/SP342.4.
Lukens, C. E., B. Carrapa, B. S. Singer, and G. Gehrels (2012), Miocene exhumation of the Pamir revealed by detrital geothermochronology of Tajik rivers, *Tectonics*, *31*, TC2014, doi:10.1029/2011TC003040.
McElhinny, M. W. (1964), Statistical significance of the fold test in paleomagnetism, *Geophys. J. R. Astron. Soc.*, *8*, 328–340.
McFadden, P. L., and D. L. Jones (1981), The fold test in paleomagnetism, *Geophys. J. R. Astron. Soc.*, *67*, 53–58.
McFadden, P. L., and M. W. McElhinny (1990), Classification of the reversal test in paleomagnetism, *Geophys. J. Int.*, *103*, 725–729, doi:10.1111/j.1365-246X.1990.tb05683.x.
McFadden, P. L., and A. B. Reid (1982), Analysis of paleomagnetic inclination data, *Geophys. J. R. Astron. Soc.*, *69*, 307–319, doi:10.1111/j.1365-246X.1982.tb04950.x.
Miall, A. D. (1977), Review of braided-river depositional environments, *Earth Sci. Rev.*, *13*, 1–62, doi:10.1016/0012-8252(77)90055-1.
Miall, A. D. (Ed.) (1978), Lithofacies types and vertical profile models in braided river deposits: A summary in Fluvial Sedimentology, *Mem. Can. Soc. Pet. Geol.*, *5*, 597–604.
Miall, A. D. (1985), Architectural-elements analysis: A new method of facies analysis applied to fluvial deposits, *Earth Sci. Rev.*, *22*, 261–308, doi:10.1016/0012-8252(85)90001-7.
Miall, A. D. (1996), *The Geology of Fluvial Deposits: Sedimentary Facies, Basin Analysis, and Petroleum Geology*, 582 pp., Springer, Berlin, New York.
Molnar, P. (2004), Late Cenozoic increase in accumulation rates of terrestrial sediment: How might climate change have affected erosion rates?, *Annu. Rev. Earth Planet. Sci.*, *32*, 67–89.
Nichols, G. J., and J. A. Fisher (2007), Processes, facies and architecture of fluvial distributary system deposits, *Sediment. Geol.*, *195*, 75–90, doi:10.1016/j.sedgeo.2006.07.004.
Nishiizumi, K., M. Imamura, M. W. Caffee, J. R. Southon, R. C. Finkel, and J. McAninch (2007), Absolute calibration of ^{10}Be AMS standards, *Nucl. Instrum. Methods Phys. Res., Sect. B*, 258–403, doi:10.1016/j.nimb.2007.01.297.
Norris, T. L., A. J. Gancarz, D. J. Rokop, and K. W. Thomas (1983), Half-life of ^{26}Al. 461 proceedings of the fourteenth lunar and planetary science conference, Part 1, 462, *J. Geophys. Res.*, *88*, B331–B333, doi:10.1029/JB088iS01p0B331.
Ori, G. G., and P. F. Friend (1986), Sedimentary basins formed and carried piggyback on active thrust sheets, *Geology*, *12*, 475–478, doi:10.1130/0091-7613(1984)12<475:SBFACP>2.0.CO;2.
Paola, C., P. L. Heller, and C. L. Angevine (1992), The large-scale dynamics of grain- size variation in alluvial basins: 1. Theory, *Basin Res.*, *4*, 73–83, doi:10.1111/j.1365-2117.1992.tb00145.x.
Pavlis, T. L., M. W. Hamburger, and G. L. Pavlis (1997), Erosional processes as a control on the structural evolution of an actively deforming fold and thrust belt: An example from the Pamir–Tien Shan region, central Asia, *Tectonics*, *16*, 810–822, doi:10.1029/97TC01414.
Raymo, M. E. (1994), The initiation of Northern Hemisphere glaciation, *Annu. Rev. Earth Planet. Sci.*, *22*, 353–383, doi:10.1146/annurev.ea.22.050194.002033.
Riba, O. (1976), Syntectonic unconformities of the Alto Cardener, Spanish Pyrenees: A genetic interpretation, *Sediment. Geol.*, *15*, 213–233, doi:10.1016/0037-0738(76)90017-8.
Robinson, A. C., A. Yin, C. E. Manning, T. M. Harrison, S. H. Zhang, and X. F. Wang (2004), Tectonic evolution of the northeastern Pamir: Constraints from the northern portion of the Cenozoic Kongur Shan extensional system, western China, *Geol. Soc. Am. Bull.*, *116*, 953–973, doi:10.1130/B25375.1.
Robinson, A. C., A. Yin, C. E. Manning, T. M. Harrison, S. H. Zhang, and X. F. Wang (2007), Cenozoic evolution of the eastern Pamir: Implications for strain accommodation mechanisms at the western end of the Himalayan-Tibetan orogen, *Geol. Soc. Am. Bull.*, *119*, 882–896, doi:10.1130/B25981.1.
Robinson, A. C., A. Yin, and O. M. Lovera (2010), The role of footwall deformation and denudation in controlling cooling age patterns of detachment systems: An application to the Kongur Shan extensional system in the Eastern Pamir, China, *Tectonophysics*, *496*, 28–43, doi:10.1016/j.tecto.2010.10.003.
Schwab, M., L. Ratschbacher, W. Siebel, M. McWilliams, V. Minaev, V. Lutkov, F. Chen, K. Stanek, B. Nelson, W. Frisch, and J. L. Wooden (2004), Assembly of the Pamirs: Age and origin of magmatic belts from the southern Tien Shan to the southern Pamirs and their relation to Tibet, *Tectonics*, *23*, TC4002, doi:10.1029/2003TC001583.

Sobel, E., J. Chen, L. M. Schoenbohm, R. Thiede, D. F. Stockli, M. Sudo, and M. R. Strecker (2013), Oceanic-style subduction controls late Cenozoic deformation of the Northern Pamir orogen, *Earth Planet. Sci. Lett.*, *363*, 204–218, doi:10.1016/j.epsl.2012.12.009.
Sobel, E. R., and T. A. Dumitru (1997), Exhumation of the margins of the western Tarim basin during the Himalayan orogeny, *J. Geophys. Res.*, *102*, 5043–5064, doi:10.1029/96JB03267.
Sobel, E. R., J. Chen, and R. V. Heermance (2006), Late Oligocene-Early Miocene initiation of shortening in the Southwestern Chinese Tian Shan: Implications for Neogene shortening rate variations, *Earth Planet. Sci. Lett.*, *247*, 70–81, doi:10.1016/j.epsl.2006.03.048.
Sobel, E. R., L. M. Schoenbohm, J. Chen, R. Thiede, D. F. Stockli, M. Sudo, and M. R. Strecker (2011), Late Miocene–Pliocene deceleration of dextral slip between Pamir and Tarim: Implications for Pamir orogenesis, *Earth Planet. Sci. Lett.*, *304*, 369–378, doi:10.1016/j.epsl.2011.02.012.
Stearns, M. A., B. R. Hacker, L. Ratschbacher, J. Lee, J. M. Cottle, and A. Kylander-Clark (2013), Synchronous Oligocene-Miocene metamorphism of the Pamir and the north Himalaya driven by plate-scale dynamics, *Geology*, *41*, 1071–1074, doi:10.1130/G34451.1.
Stone, J. O. (2000), Air pressure and cosmogenic isotope production, *J. Geophys. Res.*, *471*(105), 23,753–23,759, doi:10.1029/2000JB900181.
Strecker, M. R., W. Frisch, M. W. Hamburger, L. Ratschbacher, S. Semiletkin, A. Zamoruyev, and N. Sturchio (1995), Quaternary deformation in the eastern Pamirs, Tadzhikistan and Kyrgyzstan, *Tectonics*, *14*, 1061–1079, doi:10.1029/95TC00927.
Sun, J., R. X. Zhu, and J. Bowler (2004), Timing of the Tianshan Mountains uplift constrained by magnetostratigraphic analysis of molasse deposits, *Earth Planet. Sci. Lett.*, *219*, 239–253.
Suppe, J., F. Sabat, J. A. Munoz, J. Poblet, E. Roca, and J. Verges (1997), Bed-by-bed fold growth by kink-band migration: Sant Llorenc de Morunys, eastern Pyrenees, *J. Struct. Geol.*, *19*, 443–461, doi:10.1016/S0191-8141(96)00103-4.
Talling, P. J., T. F. Lawton, D. W. Burbank, and R. S. Hobbs (1995), Evolution of latest Cretaceous-Eocene nonmarine deposition in the Axhandle piggyback basin of central Utah, *Geol. Soc. Am. Bull.*, *107*(3), 297–315, doi:10.1130/0016-7606(1995)107<0297:EOLCEN>2.3.CO;2.
Thiede, R. C., E. Sobel, J. Chen, L. M. Schoenbohm, D. F. Stockli, M. Sudo, and M. R. Strecker (2013), Late Cenozoic extension and crustal doming in the India-Eurasia collision zone: New thermochronologic constraints from the NE Chinese Pamir, *Tectonics*, *32*, 763–779, doi:10.1002/tect/20050.
Thompson, J. A. (2013), Neogene tectonic evolution of the NE Pamir Margin, NW China, PhD dissertation, Dep. of Earth Sci., UC Santa Barbara, Santa Barbara, Calif.
Uba, C. E., C. Heubeck, and C. Hulka (2005), Facies analysis and basin architecture of the Neogene Subandean synorogenic wedge, southern Bolivia, *Sediment. Geol.*, *180*, 91–123, doi:10.1016/j.sedgeo.2005.06.013.
Vermeesch, P., C. R. Fenton, F. Kober, G. F. S. Wiggs, C. S. Bristow, and S. Xu (2010), Sand residence times of one million years in the Namib Sand Sea from cosmogenic nuclides, *Nat. Geosci.*, *3*, 862–865.
Vos, R. G., and A. J. Tankard (1981), Braided fluvial sedimentation in the lower Paleozoic Cape Basin, South Africa, *Sediment. Geol.*, *29*, 171–193, doi:10.1016/0037-0738(81)90006-3.
Wang, E., J. Wan, and J. Liu (2003), Late Cenozoic geological evolution of the foreland basin bordering the West Kunlun Range in the Pulu area: Constraints on timing of uplift of northern margin of the Tibetan Plateau, *J. Geophys. Res.*, *108*(B8), 2401, doi:10.1029/2002JB001877.
Watson, G. S., and R. J. Enkin (1993), The fold test in paleomagnetism as a parameter estimation problem, *Geophys. Res. Lett.*, *20*(19), 2135–2137, doi:10.1029/93GL01901.
Willenbring, J. K., and F. von Blanckenburg (2010), Long-term stability of global erosion rates and weathering during late-Cenozoic cooling, *Nature*, *465*(7295), 211–214.
Wolkowinsky, A. J., and D. E. Granger (2004), Early Pleistocene incision of the San Juan River, Utah, dated with ^{26}Al and ^{10}Be, *Geology*, *32*(9), 749–752.
Xinjiang Bureau of Geology and Mineral Resources (1993), *Regional Geology of Xinjiang Uygur Autonomous Region: Geological Memoirs*, Geol. House, Beijing, scale 1: 1,500,000, 841 pp.
Yang, S., J. Li, and Q. Wang (2008), The deformation pattern and fault rate in the Tianshan Mountains inferred from GPS observations, *Sci. China, Ser. D Earth Sci.*, *51*, 1064–1080, doi:10.1007/s11430-008-0090-8.
Yin, A., et al. (2002), Tectonic history of the Altyn Tagh fault system in northern Tibet inferred from Cenozoic sedimentation, *Geol. Soc. Am. Bull.*, *114*, 1257–1295, doi:10.1130/0016-7606(2002)114<1257:THOTAT>2.0.CO;2.
Zachos, J. C., M. Pagani, L. Sloan, E. Thomas, and K. Billups (2001), Trends, rhythms, and aberrations in global climate 65 Ma to present, *Science*, *292*, 686–693, doi:10.1126/science.1059412.
Zhang, P. Z., P. Molnar, and W. R. Downs (2001), Increased sedimentation rates and grain sizes 2-4 Myr ago due to the influence of climate change on erosion rates, *Nature*, *410*(6831), 891–897.
Zheng, H., C. M. Powell, Z. An, J. Zhou, and G. Dong (2000), Pliocene uplift of the northern Tibetan Plateau, *Geology*, *28*, 715–718, doi:10.1130/0091-7613(2000)28<715:PUOTNT>2.0.CO;2.
Zubovich, A. V., et al. (2010), GPS velocity field for the Tien Shan and surrounding regions, *Tectonics*, *29*, TC6014, doi:10.1029/2010TC002772.